UNIVERSITY OF CALIFORNIA
IRVINE

Discharge Flux Variability in Stored Thermal Energy Cookstoves

THESIS

submitted in partial satisfaction of the requirements
for the degree of

MASTER OF SCIENCE

in Mechanical and Aerospace Engineering

by

Michael James Bryant

Thesis Committee:
Professor Derek Dunn-Rankin, UC Irvine, Chair
Professor Yoonjin Won, UC Irvine
Professor Jack Brouwer, UC Irvine

2016

DEDICATION

In dedication to my father, for his persistent inspiration of what hard work truly means. To my mother for being an unfailing example of sincere altruism. To my brother and sister for their constant support and encouragement.

TABLE OF CONTENTS

Table of Contents

LIST OF FIGURES

LIST OF TABLES

NOMENCLATURE

Thermophysical Properties:

α	thermal diffusivity
C_p	specific heat, $\frac{kJ}{kg\,K}$
κ	thermal conductivity
ρ	density,
h_{sl}	latent heat of fusion, kJ/kg
Q	heat, kJ

Potentials:

T_{max}	maximum allowable temperature for a particular application
T_{min}	minimum allowable temperature for a particular application
T_m	melting temperature
T_0	boundary temperature
ΔT_{ch}	temperature gradient within PCM during charging
ΔT_{loss}	PCM temperature change due to storage heat leak
ΔT_{dch}	temperature gradient within PCM during discharging
ΔT_{usable}	= T_{min}- T_{max}, maximum - minimum allowable temperature
ΔT_{AB}	temperature gradient arising within the PCM
ΔT_{BD}	temperature gradient arising within fin array

Dimensionless Numbers:

$N_\alpha = \frac{\alpha_1}{\alpha_2}$ ratio of thermal diffusivities

$N_\kappa = \frac{\kappa_1}{\kappa_2}$ ratio thermal conductivities

$N_\rho = \frac{\rho_1}{\rho_2}$ ratio of densities

$\Theta = \frac{T_m - T}{T_m - T_0}$ dimensionless temperature

$\Theta_\mathrm{i} = \frac{T_m - T_i}{T_m - T_0}$ dimensionless superheating term

Dimensionless Numbers:

$\mathrm{X} = \frac{x}{L}$ position, planar phase change front

$\mathrm{S} = \frac{s}{L}$ solidification front position, planar phase change front

$\tau = \frac{\alpha t}{L^2}$ time, planar phase change front

$\mathrm{R} = \frac{r}{r_i}$ position, cylindrical phase change front

$\mathrm{S} = \frac{s}{r_i}$ solidification front position, cylindrical phase change front

$\tau = \frac{\alpha t}{r_i^2}$ time, cylindrical phase change front

$Bi = \frac{hL_c}{k}$ Biot number

$L_c = \frac{V}{A_s}$ Characteristic length

$Ste = \frac{C_{p_1}(T_m - T_0)}{h_{sl}}$ Stefan number, Dirichlet boundary condition

Subscripts:

1	solid phase
2	liquid phase
sp	specific (quantity per unit mass, kg)
c	planar or cylindrical fin array material

Acronyms:

FEM	Finite Element Modeling
IAP	Indoor Air Pollution
PCM	Phase Change Material
STEC	Stored Thermal Energy Cookstove
TES	Thermal Energy Storage

ACKNOWLEDGMENTS

I am extremely grateful for the opportunity to work on this effort. I especially would like to thank Professor Derek Dunn-Rankin for his incredible patience and always kind encouragement. The unique perspective Professor Dunn-Ranking conveyed during our discussions made this thesis possible, without taking away opportunities for me to struggle and learn on my own.

I would like to thank Professor Yoonjin Won and Professor Jack Brouwer for their support on my committee and comments on my thesis draft. You have helped shape this thesis into its current form. Thank you.

I would also like to thank my collaborators in the UCI Department of Economics, Debapriya Chakraborty and Professor Linda Cohen for their support of this work. Your insights were invaluable to the success of this effort.

I cannot appreciate more the support from members of the international improved cookstove community. Particularly Priyadarshini Karve of Samuchit Enviro Tech, R.S. Deshmukh of the Appropriate Rural Technology Institute (ARTI), Anurag Bhatnagarnd of the Self Employed Women's Organization (SEWA), and Patrick Sherwin of GoSun stove. Your insights were transformative and your willingness and excitement to discuss the novel concept in this thesis I will not soon forget.

Many thanks to the Bill and Melinda Gates Foundation for funding the work under their Grand Challenges Explorations (GCE) Grant program [OPP1097505]. Without their support of novel research paths in global development this thesis would not exist.

I am grateful as well for all the students who have assisted on the project over the last couple years, and the many friends and family that have encouraged me along the way. Thankyou!

ABSTRACT OF THE THESIS

Discharge Flux Variability in Stored Thermal Energy Cookstoves

By:

Michael James Bryant

Master of Science in Mechanical and Aerospace Engineering

University of California, Irvine, 2016

Professor Derek Dunn-Rankin, Chair

A thermal analysis and test is performed to determine flux and temperature variability for phase change thermal energy storage to investigation feasibility of use in a Stored Thermal Energy Cookstove (STEC). The phase change material (PCM) $NaNO_3 - KNO_3$ Eutectic (52: 48) Solar Salt is identified for energy storage in STEC due to a melting temperature of 222°C which is deemed appropriate for use in cooking up to temperatures of 200°C $\pm$ 20 °C. 1-D planar and cylindrical analytical multiphase solutions are correlated with a transient non-linear ANSYS Finite Element Model (FEM). 1-D idealized models of planar and cylindrical analytical multiphase solutions show the flux stability of cylindrical solidification is twice that of planar solidification. Flux drops a linear average of 0.5%/min in the last half hour of a one hour cooking session in cylindrical solidification vs 1%/min in planar solidification under a constant temperature (dirichlet) boundary condition of 42 °C below the melting point of the PCM. Solidification progresses more quickly in the planar case yielding a solid PCM thickness of 3.3 cm after one hour vs 2.4 cm in the cylindrical case. A test is performed on a simplified STEC apparatus to investigate cooling rates of the

cooking surface while boiling water. 0.5L of water is brought to boil from room temperature with a linear average cooking surface flux of 21,000 W/m^2 and a cooking surface cooling rate of 3.8 ℃/min. Results show increasing the thermal conductivity of the PCM and reducing the total thickness of the solidifying PCM layer before and after discharge will reduce cooling rates, improve stability of the flux delivery device, and increase feasibility of use. Pursuing lower flux cooking and non-cooking applications may increase likelihood of adoption by reducing thermal gradients during discharge. A proposal to explore further development of STEC to aid adoption is discussed.

Chapter 1: Introduction

1.1 Motivation

The World Health Organization (WHO) estimates that nearly three billion people around the globe do not have access to a modern method of preparing their meals. For rural communities the daily task of cooking often requires burning wood, dung, or other heavily emitting biofuels in an open fire. Figure 1.1 shows a three stone stove which is a traditional method of cooking found in some regions. Relying on an open fire for cooking heat has consequences in three categories.

1. *Heavy labor demands for women* - in some regions women are required to perform 5-8 hours of manual labor every day, with an estimated 20 percent of that time dedicated to collecting fuel for cooking[1].

Figure 1.1 Example of a traditional cooking method called a Three Stone Stove. A Three Stone Stove is simply 3 bricks, concrete blocks, or stones arranged such that a fire can burn beneath a pot without the pot obstructing airflow to the fire.

2. *Health threat for the poor* – depicted in Figure 1.2, WHO data examines the impact of biofuel cookstoves with the Disability Adjusted Life Years (DALYs) metric, which is a measure of years of life lost or hindered due to poor health, disability, or premature death. WHO estimates 4.3 million people die annually around the globe from diseases associated with emissions from biofuel burning cookstoves [2].

3. *Global environmental stress* - heavy reliance on burning biofuels for cooking heat exacerbates deforestation and puts pressure on the Earth's climate through the release of additional greenhouse gases.

1.1.1 A Need for Cleaner Stoves

Previous work has clearly established that there is an acute need for an alternative cooking method in rural communities; however, many challenges have prevented a versatile

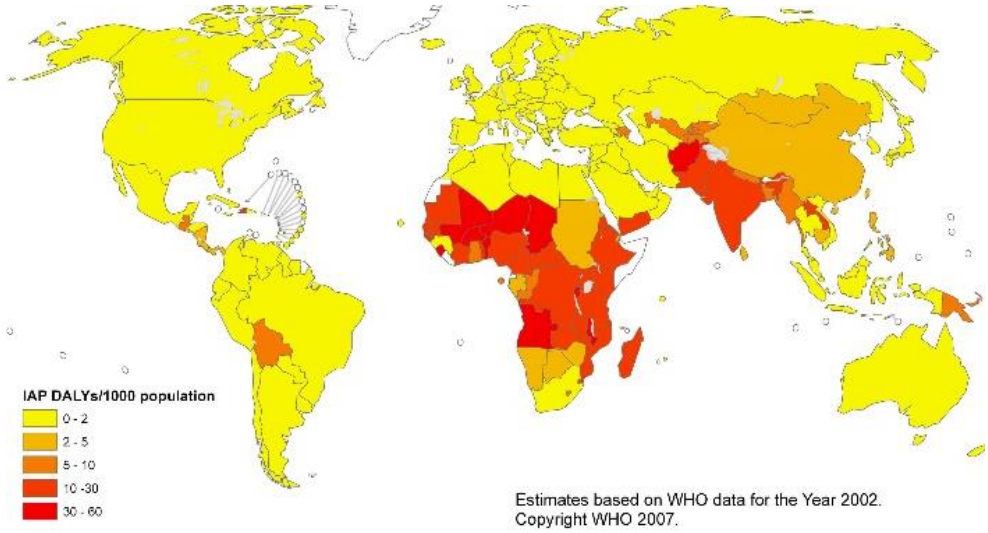

Figure 1.2 World Health Organization map of disability adjusted life years from indoor air pollution around the globe. The most impacted regions (in red) are developing countries [2].

Figure 1.3 Examples of more efficient biofuel burning cookstoves. Efficiency is improved by constricting the air inlet to the combustion zone which leads to a higher velocity draft, improving oxygen supply and increasing combustion efficiency [32].

replacement for traditional cookstoves. The main challenges include a need to develop a cost effective alternative that utilizes local resources, is reliable with little or no maintenance, fits into established cultural cooking preferences, and, most importantly, saves millions of lives by reducing harmful emissions. Prior and current effort is particularly focused on exploring cleaner biofuel burning cookstoves, including efforts to improve the ventilation of the cookstove as well as the efficiency of combustion [3]. Figure 1.3 shows examples of improved biofuel stoves that are currently on the market. Unfortunately, the potential of reducing emissions for biofuel stoves is limited fundamentally because combustion and an open flame are necessary for release of cooking heat. Furthermore, the most impacted regions have limited access to clean biofuels and therefore must rely upon burning heavily emitting fuels such as wood, dried dung, farm plant matter, or in some cases trash. Turning away from heavily emitting biofuel combustion is desirable, however, the typically available alternatives, such as natural gas, liquefied petroleum gas (LPG), and electric stoves, are expensive and require a significant investment in infrastructure.

Despite the drawbacks of burning biofuels for cooking heat, widespread use of combustion can be partly attributed to the ease of cooking with this method. Cooking technologies are designed to allow the controlled transfer of heat from a heat source to food. Cookstoves can therefore be considered *thermal flux delivery devices*, where the cookstove is used to deliver a thermal flux at a required rate for a required period of time. Control of thermal flux, and therefore heating power, is achieved by controlling the temperature of a heat source. The heat source takes many different forms. With an open flame source, heat is transferred through convection and radiation from the flame and coals. An open flame biofuel cookstove achieves flux control by changing the quantity of fuel burned. In the case of a traditional biofuel stove this would mean adding or removing solid fuel to increase or decrease the heating rates depending on the food being cooked. Since adding fuel can be done manually, no additional equipment is required to achieve control over heating rates.

Other open flame stoves that burn cleaner fuels, such as liquid or gas fuel stoves (natural gas, LPG, etc.) also achieve flux control by varying the quantity of fuel burned. For a non-combustion based cookstove such as electric stove or griddle, heat transfer is dominated by direct conduction to the food, and flux control is achieved by varying the power delivered to a resistive or inductive heater, which controls the temperature of a surface. These methods of cooking offer less emissions; however, they typically require specially designed stoves and/or cookware along with an infrastructure to deliver gas or electricity. The increased cost and infrastructure requirement places them out of reach of many rural communities.

1.1.2 Solar Stoves

Another class of stoves are solar cookstoves. Solar cookstoves rely on concentrating an emissions free and renewable heat source, the sun, as an alternative to burning biofuels for cooking heat. Current solar cookstoves, however, require direct sunlight to cook, limiting their use to clear sunny days and daytime hours. Figure 1.4 shows an example of a typical portable solar cookstove. Since it is often desirable to cook a meal in the morning before sunrise or late evening after sunset, the need for sunlight is a severe limitation. Additionally, current solar cookstoves are not able to adjust their cooking temperature on demand. A potential new capability for solar cookstoves, and the focus of this thesis, is the integration of Thermal Energy Storage (TES) and heat rate control. Integrating TES into a solar cookstove would allow for storage of heat from intermittently available heat sources so the thermal energy can later be released in a controlled manner. Solar energy has no emissions, is renewable, and is freely available; and thus is a great potential alternative to burning biofuels. Adding energy storage to solar cookstoves could enable widespread use of solar heat for cooking and providing controlled discharge of TES in general may also enable

Figure 1.4 The HotPot Solar Cooker (left)[33][34] and the GoSun Stove (right) are examples of small solar cookstoves. Sunlight is reflected and concentrated on a dark inner container that is housed within an optically transparent outer layer. The arrangement creates an enhanced greenhouse effect that can achieve temperatures exceeding 200 °C. The vacuum insulated GoSun Stove can reach temperatures approaching 300 °C.

applications in rural communities beyond cooking; including room heating, dehydrating, keeping food warm, and uses not yet conceived.

1.1.3 Thermal Energy Storage (TES)

Chemical TES

A fundamental challenge to enable TES for solar cookstoves is determining the optimal method of storing heat. Extensive research exists on the use of a variety of materials in TES. All methods can be categorized as either mechanical or chemical. Chemical TES includes reversible chemical reactions such as the hydration of salt hydrates and acids, deoxygenation of metal oxides, and decomposition of metal carbonates, among others [4]. Thermochemical

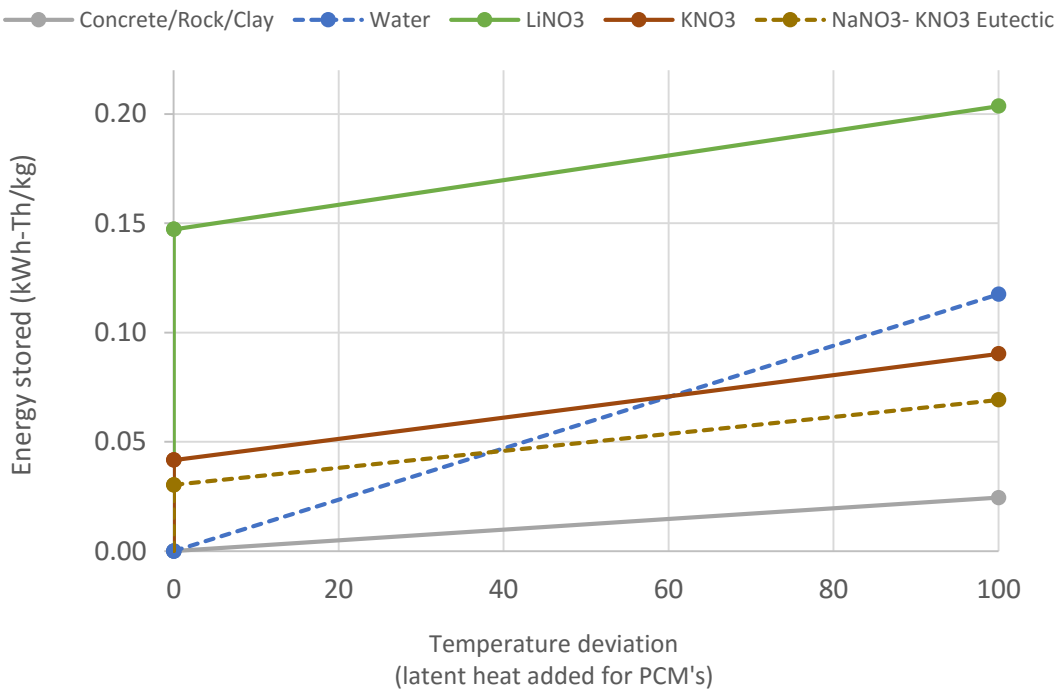

Figure 1.5 Depicted in this chart is the specific energy stored in select phase change materials plus the sensible heat stored over a temperature region around the melting point. Since boiling water is a common activity and a reasonable proxy for many cooking activities (rice, curry, lentils, etc.), water is included for comparison.

storage typically requires pumps and containment systems to manage multiple reactants that are often toxic. The materials required are therefore costly, but chemical thermal storage has received increased attention due to a high specific energy density relative to other TES methods and the ability to store thermal energy for long durations with minimal losses [5]. Due to the high cost, safety challenges during handling, and complexity for small scale modular applications, like that required for an off-grid rural application, chemical thermal storage is not considered in this thesis. However, future work should address the appropriateness of chemical thermal storage for cooking applications in greater depth.

Mechanical TES

Mechanical storage methods include sensible heat and latent heat storage with latent heat methods involving a Phase Change Material (PCM) that undergoes a solid-liquid, liquid-gas, or solid-solid phase transition [6]. Latent heat storage methods are attractive because they have a stable temperature during energy release around the melting point of the chosen PCM. There is also a wide array of PCM's available whose properties have been studied in detail [6]–[9]. An ideal TES system of any type maximizes heat storage per unit mass and volume. Thus, maximization of specific and volumetric energy density is desired. Utilizing the liquid-to-solid phase change of carefully selected materials enables significantly higher energy density than a TES system that utilizes only sensible heat, potentially reducing the cost of heat storage (Figure 1.5).

1.1.4 Stored Thermal Energy Cookstove (STEC)

Solar stoves that utilize a liquid-to-solid phase change material to store heat for cooking after dark have been proposed but have received limited study [10]. No large-scale sustained use has been demonstrated and no optimization or design fundamentals have been presented. Understanding the potential of a Stored Energy Solar Cookstove (STEC) begins with an approximation of the energy and temperature requirements of typical cooking activities. These thermodynamic requirements will dictate PCM and encapsulation material selection. Table 1.1 contains the specific energy and the temperature required for common cooking activities across India, a country that has a large rural population base with a particularly acute need for alternatives to traditional biofuel burning cookstoves[1]. For cooking the desire is for a PCM that melts above 200 $°C$ and that is commonly available and therefore inexpensive. Examples of materials that fit these requirements are listed in Table 1.2. Nitrate salts including the eutectic mixture of $NaNO_3$ - KNO_3, otherwise known as Solar Salt, have received considerable study [7], [8], [10]–[13]. Because of extensive industry experience with Solar Salt and the balance between its melting temperature of 222 $°C$ and its availability, the goal of this thesis is to match the heat flux requirements of cooking using thermal energy stored in a eutectic mixture of $NaNO_3$ - KNO_3, recommend a conceptual design of STEC that balances thermal performance with observations of user needs, and identify any remaining obstacles to the widespread adoption of STEC.

Table 1.1 Temperature and heat requirements of select cooking activities [35].

Activity:	*Boil Water (1 Liter)*	*Rice, Dal, Boiled Vegetables*	*Chapati's (1 Meal)*
Temperature Req. (°C)	200	200	330+
Energy Req. (kWh-Th/kg)	0.094	0.100	0.116

Table 1.2 Melting point, thermal conductivity, and cost of select phase change materials.

	Melting Point (°C)	*Cost ($/kg)*
Sodium Nitrate ($NaNO_3$)	308	~0.50
Potassium Nitrate (KNO_3)	334	~1.00
$NaNO_3$ - KNO_3 Eutectic "Solar Salt"	222	~0.70
Lithium Nitrate ($NaNO_3$)	255	~5

1.2 System and Design Evaluation

1.2.1 Design Iterations

Significant effort building the fundamental understanding of cooking using thermal energy storage at The University of California Irvine (UCI) began under the advisement of John Garmen in 2013 after he received a Phase I Bill & Melinda Gates Foundation Grand Challenges Explorations Grant. The UCI Stored Energy Solar Stove Project performed a concept study and evaluation to determine the technical feasibility of storing solar heat energy in a phase change material for use in cooking. In the first year a mixture of graduate and undergraduate students researched materials for thermal energy storage and built the 1st generation prototype of STEC, shown in Figure 1.6. A key lesson learned from the first generation stove was the difficulty of extracting heat from the salt due to its low thermal conductivity. These insights informed the design of a 2nd generation stove. During 2014-2015 under the advisement of Professor Derek Dunn-Rankin, the author oversaw testing of the second generation stove with a new team of undergraduate and graduate students and led subsequent efforts focused on the objectives listed below.

1. Determine the fundamental limitations of storing and extracting heat from phase change materials. (temperature stability, heating rates, weight, volume, cost, etc.).
2. Determine the temperatures and power requirements of different cooking activities.
3. Determine the needs and expectations of users.
4. Determine if STEC can provide users their expected cooking performance.

Design Iteration	Tests Performed	Key Outcomes
1st Generation (2013)	**Cooking Experiment (Frying)**	**Outcomes** • Capable of cooking bacon, eggs, and other fried foods. • Storage duration is 4 hours. **Challenges:** • PCM insulates cooking surface during solidification. • Flatness of cooking surface was not carefully specified which insulated the pan from the cooking surface. • Insulation effectiveness of must be improved to increase storage duration.
2nd Generation (2014)	**Melting Experiment**	**Modifications from 1st Gen:** • Bonded a high thermal conductivity core to the heat spreader to prevent PCM from insulating cooking surface as it solidifies. • Spherical geometry is optimized for a high volume to surface area ratio for increased insulation effectiveness. **Outcomes** • Tested melting times using a solar concentrator. • Test details contained in a M.S. Project report by Stuart Foster [36].

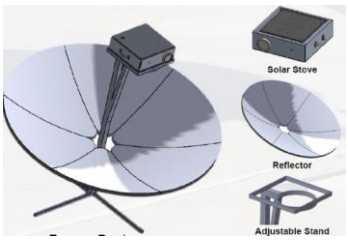

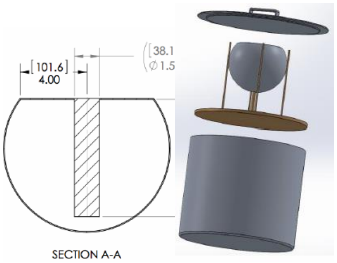

Figure 1.6 The first and second design iterations of the UCI Stored Thermal Energy Cookstove.

Design Iteration	Tests Performed	Key Outcomes
3rd Generation (2015)	**Water Boiling Test**	**Modifications from 2nd Gen:** • Cylindrical geometry selected for simplicity and ease of manufacture. • Pin fin array of aluminum rods is inserted into the PCM and bonded to the cooking surface. • A vacuum insulated thermos is used to provide compact insulation. **Outcomes** • Boils 0.5 L of water in 20 min and simmers for 30 min.

Figure 1.7 Third design iteration of the UCI Stored Thermal Energy Cookstove.

Insights gained in answering questions (1) and (2) are detailed in later chapters of this thesis. Testing of the 2nd generation stove led to recognition that understanding user interaction was required to evolve the design further. Thus, to answer questions (3) and (4) a collaboration with the UCI Department of Economics was pursued to develop a flexible pilot strategy for potential STEC technology adoption. The author visited multiple rural

Figure 1.8 In Jadhavwadi, a village outside of Pune, Maharashtra, women build and sell improved concrete biofuel cookstoves.

Figure 1.9 Examples of cookstoves that we observed during our visit to India.

communities in India over a 10-day period in September 2015 with a UCI Department of Economics colleague, Debapriya Chakraborty, to evaluate the likelihood of adoption in a rural setting. Figure 1.8 shows a photo from one of the villages visited. Traveling to rural villages allowed impartial observation of performance expectations for cookstoves of any kind; enabling identification of the labor burden relieving potential of STEC. Also, to develop a deployment strategy there was a need to visit locations where we would find potential users of the technology. We chose to visit India due its large rural population and the existence of organizations that already have extensive experience with sustainable deployment and adoption of rural technologies. Villages in Maharashtra and Gujarat were visited. Figure 1.9 shows photos of different cookstoves that we observed. A field visit also provided an opportunity to meet with local organizations. The 3rd generation of STEC was developed to be a compact demonstration of cooking using stored solar energy. During our visit we met with representatives of Samuchit Enviro Tech, The Appropriate Rural Technology Institute (ARTI), and the Self Employed Women's Association (SEWA). We

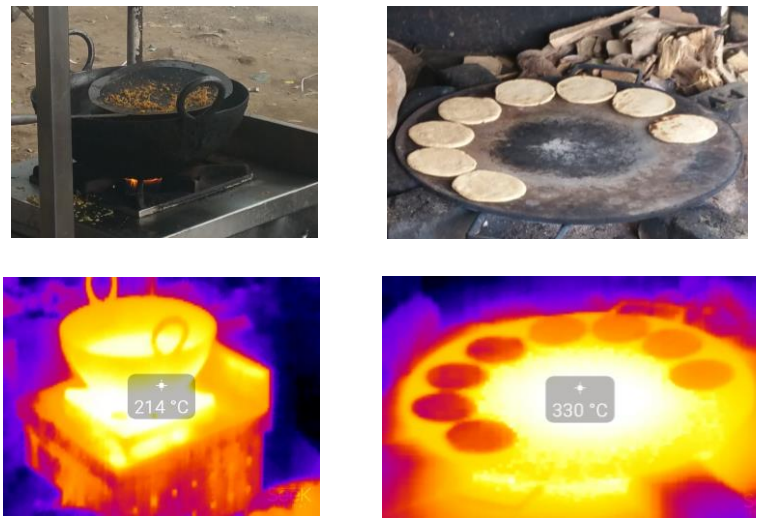

Figure 1.10 Thermal photos of deep frying (left) and a large chapatti cooktop (right). Note the large thermal gradients in the chapati cooktop (200 ℃ at edges) and the high peak temperature (330 ℃ is the limit of the Seek CompactXR USB Thermal Camera used to capture the photos above).

demonstrated the 3rd generation of STEC and conversations with these organizations were critical in informing the next evolution of the system. We observed a wide variety of cooking methods in the commercial and home setting and took thermal photos using a Seek CompactXR USB Thermal Camera. Figure 1.10 contains two examples of commercial scale cooking operations we observed. An important outcome from these images is the ability to measure the temperatures required to cook a variety of foods in a natural setting without impeding the cook's normal behavior. Observations of high peak temperatures (in excess of 330 ℃) and large temperature gradients (greater than 130 ℃) in cooking surfaces is a critical insight. Since cooking routines are typically passed down through generations and ingrained culturally. STEC must provide peak similar temperatures and temperature gradients as the photos depicted in Figure 1.10. If this is not the case, the cooking experience of STEC may differ drastically from user expectations, hindering the likelihood of adoption.

1.2.2 STEC: 4th Generation Modular Design

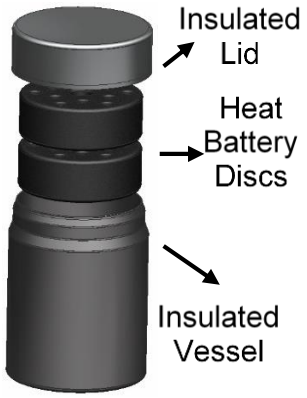

Figure 1.11 Primary Components of a Stored Thermal Energy Cookstove (STEC)

Field observations informed the design of a cookstove that can explore complications related to user adoption while simultaneously advancing technical understanding. The efforts of the previous two years of the Stored Energy Solar Stove project at UCI have demonstrated that it is technically feasible to cook on stored solar energy. In November 2015 an application was submitted to the Bill & Melinda Gates Foundation to continue developing STEC and the core technical understanding simultaneously with an understanding of users. Proposed to the Gates Foundation was the combination of a novel technology shown in Figure 1.11 and Figure 1.12 along with a flexible pilot strategy that enables a systematic approach to effectively mature thermal energy storage into practical and modular labor saving devices, and deploy them at scale.

STEC could enable utilization of renewable heat sources, such as sunlight, in cooking even after sunset. Confirmed by direct conversations with potential users, replacing traditional biofuel cookstoves with solar thermal cookstoves could substantially increase labor productivity of rural women by reducing or eliminating the 1-2 hours daily they spend

collecting biofuels (wood, dung, etc.). Our Phase I study showed that, coupled with a heat source like a solar concentrating dish, STEC can considerably reduce biofuel combustion as a source of heat and cooking in rural communities where approximately 3 billion people globally now rely on solid fuels. In addition to reducing labor demands, successful development of STEC would reduce the exposure of women to cooking fire emissions, estimated by the World Health Organization to cause 4.3 million premature deaths annually. Finally, STEC can reduce deforestation and the climate stress associated with current reliance on biofuels as a source of heat.

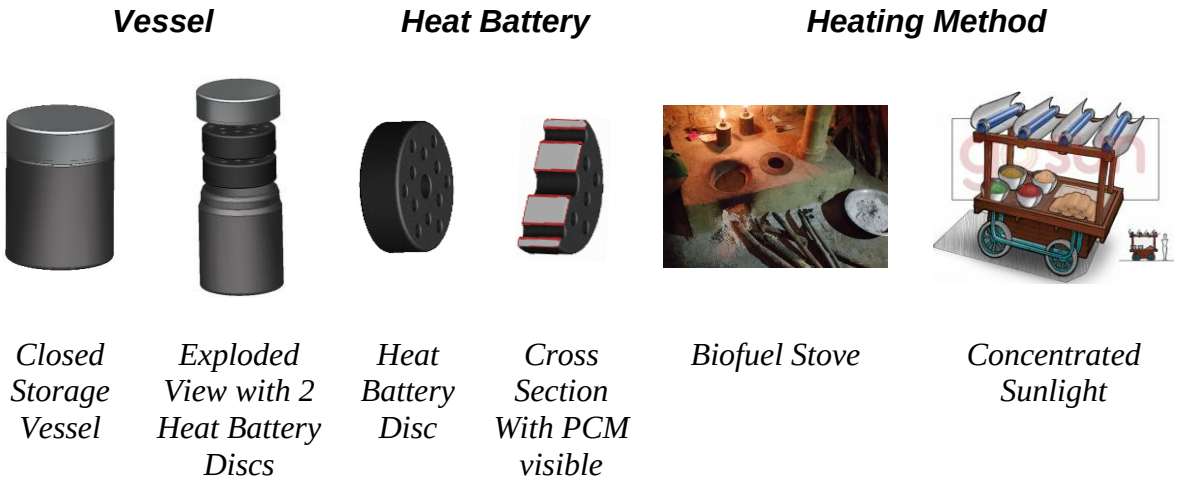

Figure 1.12 Full system required for STEC. The heat battery disc charging method is flexible, either biofuel combustion or concentrated sunlight can be the heat source.

Chapter 2: Methodology

As demonstrated in Chapter 1, an effective alternative rural cookstove requires a compact medium for thermal energy storage as well as control of thermal flux. This combination demand leads to a thermal design challenge for a PCM thermal energy storage system that is the core of this thesis. The PCM energy density and performance comparisons made in previous sections are simple approximations based on bulk material properties. Detailed heat transfer behavior has not yet been taken into account. The curves plotted in Figure 1.5 were generated with a lumped capacitance model based on Equation (2.1).

$$Q_{sp} = C_p \Delta T_{\text{usable}} + h_{sl} \tag{2.1}$$

Where Q_{sp} is specific energy, ΔT_{usable} indicates the temperature deviation around the melting point of the PCM, and C_{p} and h_{sl} are the specific heat capacity and solid to liquid heat

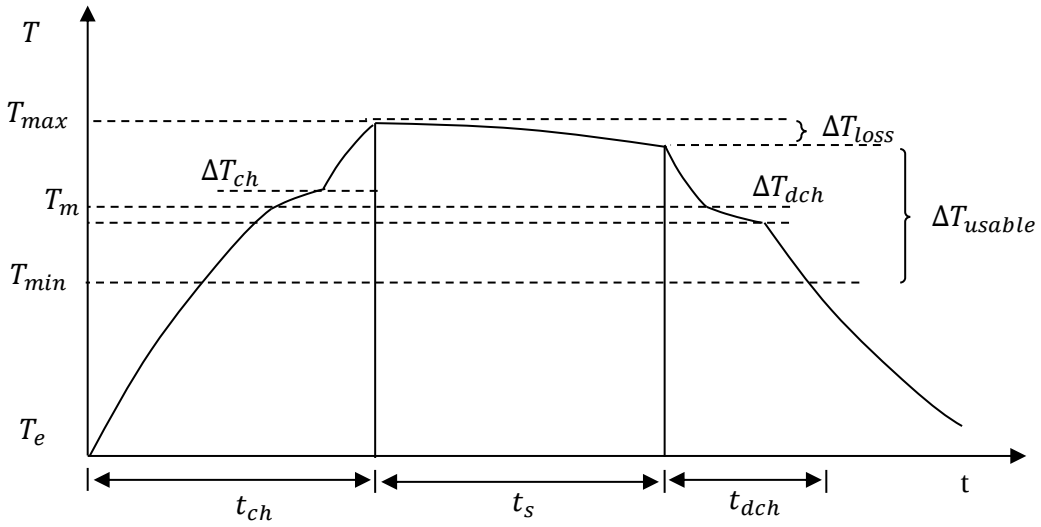

Figure 2.1 Qualitative average PCM temperature for a latent heat thermal energy storage system over time. ΔT_{ch} and ΔT_{dch} indicate temperature gradients within the phase change material during charging and discharging periods, respectively.

of fusion of the PCM, respectively. The sensible heat contribution from a PCM TES system is important to consider since despite more rapid temperature changes after phase change, some applications could make use of the sensible heat content. Recall that the motivation of utilizing a PCM is because it serves as a constant temperature energy "reservoir" during charging and discharging. While this can be an approximately accurate assumption, constant temperature only truly exists at the phase boundary. Temperature gradients within a PCM will always arise during solidification and melting. Shown in Figure 2.1 is a qualitative plot of average PCM temperature during "charging", "storage", and "discharge" of heat from a PCM. There will always be variation in the average temperature of the PCM during melting and solidification due to temperature gradients that arise within the PCM. The magnitude of these gradients will depend on the geometry, material properties, and the thermal flux requirements of the particular application.

2.1 Quantifying Thermal Gradients

Effectively charging and discharging thermal energy from a phase change material depends on the ability of the encapsulation method to allow heat to flow out of the phase change medium without manifesting large thermal gradients. As is apparent from Table 2.1, the thermal conductivity of PCM's are typically very low [14]. Encapsulation techniques therefore require interfacing the PCM with a medium that has a high thermal conductivity. Containing the PCM within a spherical shell, or interfacing it with an array of planar, cylindrical, or curved fins, a lattice, or foam have all been proposed [15]–[22]. Another method is to improve the thermal conductivity of the PCM through the addition of high

thermal conductivity filler materials [23]. Regardless of the method, the desire is to increase the bulk average thermal conductivity of the combined container and PCM system in the direction of dominant heat flow, therefore reducing the gradients in the PCM during charging and discharging. In contrast to Equation (2.1), due to thermal gradients the heat storage potential in a realistic thermal storage device will be given by Equation (2.2).

$$Q_{real} = Q_{ideal}\eta < 1 \tag{2.2}$$

Where η is a value greater than zero but less than one that indicates a ratio of the maximum possible extractable heat over the ideal (Q_{real}/Q_{ideal}). The value for η will be approximately 1 only if a PCM remains isothermal during phase change. Quantifying the degree of non-

Table 2.1 Thermophysical properties of selected PCMs used in TES.

Material	T_m	C_{p_s}	C_{p_l}	ρ_s	ρ_l	h_{sl}	κ_s	κ_l	Source
Rock		0.879		1600-2560					[6],[4]
Brick		0.840		1600-1920			0.72		[6],[37]
Concrete		0.880		1900-2400					[4],[37]
Water	0	2.04	4.23	920	1000	333.7	1.88	0.569	[6],[38]
Engine Oil			1.880		888			0.145	[6],[37]
$LiNO_3$	252	2.03		2130		530	1.33		[4],[37]
$NaNO_3$									
KNO_3	337	1.75		1860		150	0.43		[4]
NaCl	800	0.95		2160		520	4.0		[4]
$NaNO_3$-KNO_3 Eutectic (52:48)	220-222	1.6	1.4	1800	1700	109	0.8		[8], [10][7]
Aluminum	n/a	0.90	n/a	2700	n/a	n/a	167	n/a	

Note: T_m, PCM melting temperature [°C]; $C_{p_{s\,or\,l}}$, specific heat capacity of solid or liquid phase, $\left[\frac{kJ}{kg\,K}\right]$; $\rho_{s\,or\,l}$, density of solid or liquid phase, $\left[\frac{kg}{m^3}\right]$; h_{sl}, enthalpy of liquid to solid phase transition, $\left[\frac{kJ}{kg}\right]$; $\kappa_{s\,or\,l}$, thermal conductivity of solid or liquid phase, $\left[\frac{W}{m\,K}\right]$

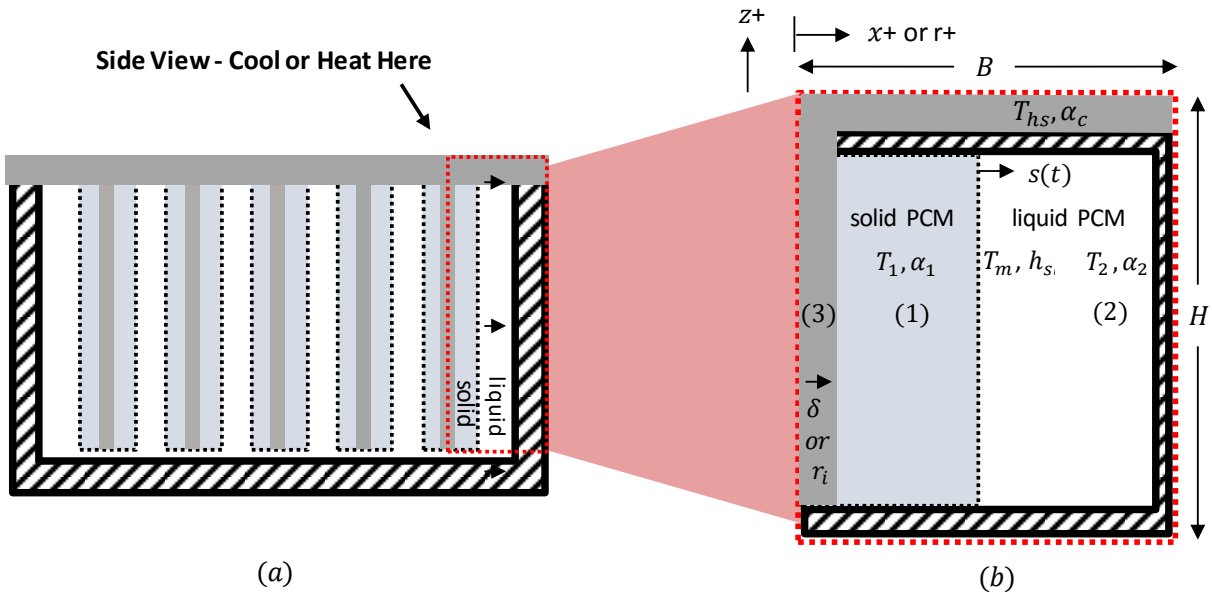

Figure 2.2 (a) Cross section of a PCM TES container with planar fins interfaced with the PCM and (b) a control volume of a representative phase change energy storage element with three distinct regions; (1) solidified PCM, (2) liquid PCM, and (3) an interfacing element of an array of planar cylindrical pin fins with a thickness of δ, or cylindrical pin fins with a radius of r_i.

isothermal behavior requires a summating of the thermal gradients along the heat transfer path within a generic thermal energy storage element. Since temperature stability during discharge is important for cooking applications, quantifying gradients during discharge is key. Figure 2.2 is a snapshot during a discharging process for a phase change storage element. Recall that while the temperature is constant during a liquid-to-solid phase change; constant temperature only exists at the evolving phase change front. In Figure 2.2 (b) there are three regions that have independent material properties and distinct temperature distributions. The key consideration is how the thickness of the evolving solid layer of PCM will impact the temperature of the heat spreading surface, T_{hs}, with time. Figure 2.3 depicts the qualitative evolution of the average PCM temperature, T_{PCM}, and T_{hs} over time. During solidification T_{hs} will always be lower than the average PCM temperature. The limits T_{max} and T_{min} indicate the maximum and minimum temperature allowed for the particular

application. For example, in the case of cooking, an average of these limits would be a cook's set point. The allowed variation around the set point without significantly altering the cooking experience is bounded by T_{max} and T_{min} which in a rural setting a cook would know from experience and intuition. From field observations the allowable variation is approximately 20 °C for cooking around 200 °C.

Quantifying and minimizing ΔT_{ABCD} while simultaneously maximizing flux in Figure 2.3 is required. These goals are directly in conflict. Material properties of the fin and PCM jointly imply an optimum fin spacing, length, and fin shape for the assembly. Design of what is effectively a finned heat sink is well understood and routine for applications where the heat sink is immersed in air (or other heat transfer fluid) and the heat transfer coefficient on the

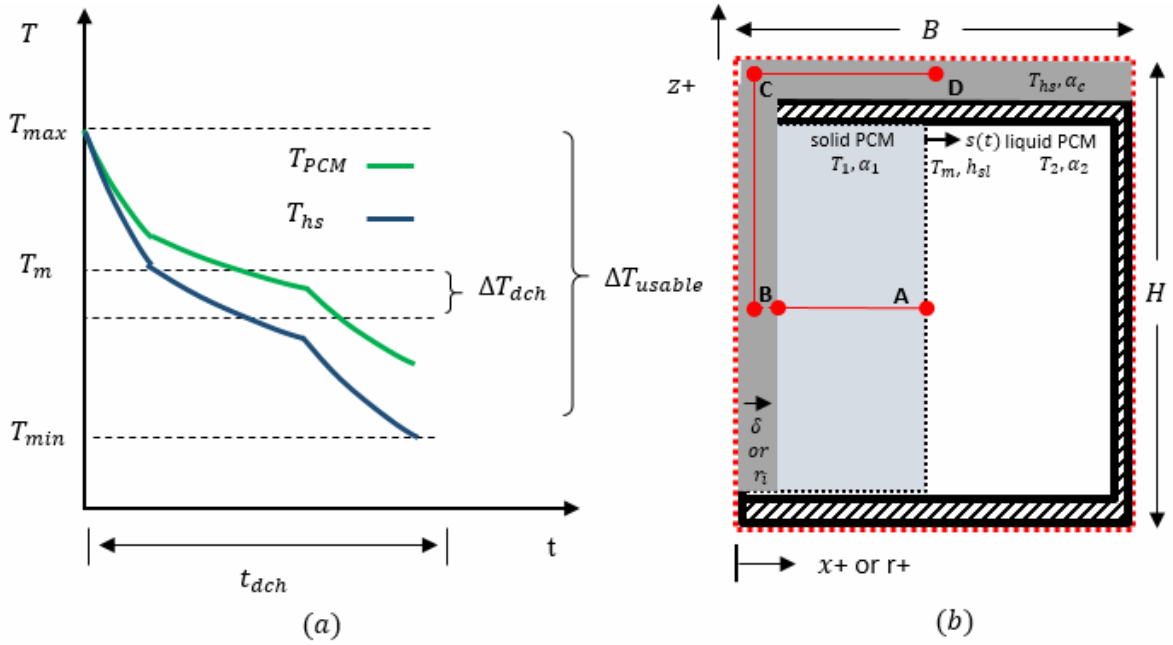

Figure 2.3 (a) Qualitative (not explicitly generated from an equation) evolution of key temperatures within a thermal storage element and (b) a representative control volume within a PCM heat storage device with a heat path depicted. During solidification a temperature gradient, ΔT_{ABCD}, will develop along the path ABCD such that $T_A = T_m = T_{hs} + \Delta T_{ABCD}$ with $T_{hs} \approx T_D$.

fin to fluid interface is driven by free or forced convection and thus known *a prior* [24]. In the case of a liquid medium undergoing a solid to liquid phase change the scenario is quite complex. The complete temperature distribution includes three unique regions that are functions of time and at least two spatial dimensions. The functions that describe each region are non-linear and non-steady. Assumptions are required to allow for a simplified 1-D analysis in each region that can later be combined to determine ΔT_{ABCD} and a value for the variability in the flux.

2.1.1 Conduction Dominated Solidification

The temperature distribution in the liquid PCM region can be described utilizing the fundamental heat transfer relation. The question arises whether the solidification process is conduction controlled or convection controlled. In a convection controlled phase change process the solidification front will form a curved shape and therefore the region will be 2-D [25]. The driving parameter that determines hydrodynamic stability in the liquid for the control volume in Figure 2.3 (b) is the Rayleigh number shown in Equation (2.3).

$$Ra = \frac{g\gamma(T_{x=B} - T_m)}{\nu\alpha} B^3 \tag{2.3}$$

Where g is the local acceleration due to gravity, γ, ν and, α are the coefficient of volumetric expansion, kinematic viscosity, and thermal diffusivity of the melt, respectively. B is the characteristic length of the cavity. Prior work reports a "conduction limit" Rayleigh criteria of 10^4 or less [26]. For a process that contains a shear free surface on one side the limit is $Ra \leq 10^3$ [27]. Since a vessel containing a PCM will have an air gap on one side to allow for expansion and contraction during phase change, modeling the process with one shear free

surface is appropriate. For any value of Rayleigh number below the conduction limit the fluid will be stationary and heat will transfer through only conduction. Typical values for Rayleigh number for the materials in Table 2.1 are O (10^6). Thus, the Rayleigh number will be below the conduction limit with either cavity sizes on the order of $10^{-3}\ m$ or with small thermal gradients in the melt. Small thermal gradients are present in what is referred in the literature as a Stefan or one region problem [28],[19]. The scenario involves a solidification process where the liquid begins uniformly at the melting temperature of the PCM. As the liquid solidifies, it remains at the melting temperature, thus no thermal gradients arise in the liquid. Understanding in detail the temperature and flux stability of the Stefan problem focusing on a 1-D thermal model provides key insights.

2.2 1-D Heat Transfer Model

Figure 2.3 depicts a heat transfer path ABCD. The temperature gradient along this path can be solved piecewise with a distinct solution for each region. Figure 2.4 shows a simplified heat transfer path that consolidates the path based on common materials. The total gradient due to phase change during discharge, ΔT_{dch} in Figure 2.3, is the summation of the gradients in Equation (2.4).

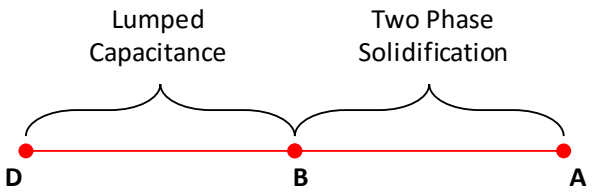

Figure 2.4 Simplified heat transfer path for a thermal storage element. Ideally $\Delta T_{ABCD} \approx 0$.

Where ΔT_{AB} is the temperature gradient within the PCM between point A and B and ΔT_{BD} is the gradient within the heat spreader and fin array between point B and D. The heat capacity of the vessel and fin array will be much less than the heat capacity of the PCM. Thus the heat transfer process within element BD is assumed as pseudo-steady. The gradient in the high conductivity element can be approximated using a 1-D lumped capacitance model with Fourier's law of conduction given in Equation (2.5).

$$\dot{q_{BD}}(x) = -k\frac{\partial T}{\partial x} \tag{2.5}$$

where $\dot{q_{BD}}(t)$ is the flux within line segment BD. $\dot{q_{BD}}(z,t)$ will vary in time based on the changing flux at point B, which is determined by the multiphase solidification problem in region AB.

2.2.1 Multiphase Heat Transfer Solutions

As previously discussed, the simplest phase change (solidification or melting) scenario is one where a single material begins uniformly at a temperature, T_m, in a container with adiabatic walls on all sides except one. Such a boundary condition leads to the evolution of a uniform, 1-D solidification front. Generally, however, a phase change process could include some heating or cooling beyond the melting point. Thus, the initial temperature for the material might be some value, $T_i > T_m$. Known as the Neumann or two-region problem, it is so named because for a complete solution a time dependent temperature distribution in *two* regions (the liquid and solid phase) must be described. The solution to the Neumann problem is not significantly more complex than the Stefan problem and the Stefan solution is easily

recoverable from the Neumann solution by setting $T_i = T_m$ in the Neumann solution. For this reason, the solution to the Neumann problem will be given [29]. For the following solution, it is assumed the material has a distinct melting temperature, all thermo-physical properties are isotropic, and heat transfer is conduction dominated. The boundary at the non-adiabatic wall is constant temperature (Dirichlet BC) set at some time $t > 0$. Special attention is paid to planar (Figure 2.5) and cylindrical (Figure 2.6) solidification fronts, since these are the most commonly proposed geometries for fins interfacing with a PCM.

2.2.1.1 Planar Dominated Solidification

The following solution describes the behavior of the solidification process for a 1-D planar geometry. This is the solution to the basic element for a container with an array of planar fins like that depicted in Figure 2.5. The solution begins with the energy equation in Cartesian coordinates given in Equation (2.6) [30]. Thermophysical properties are assumed constant and effects due to expansion of the solid are ignored.

$$\frac{\partial T}{\partial t} + v_x \frac{\partial T}{\partial x} + v_y \frac{\partial T}{\partial y} + v_z \frac{\partial T}{\partial z} = \alpha \left[\frac{\partial^2 T}{\partial x^2} + \frac{\partial^2 T}{\partial y^2} + \frac{\partial^2 T}{\partial z^2} \right] + \frac{H_v}{\rho C_p} \tag{2.6}$$

Under a condition of a static fluid with conduction dominated heat transfer and no internal heat generation, the energy equation simplifies to the 1-D heat equation shown in Equation (2.7).

$$\frac{\partial T}{\partial t} = \alpha \frac{\partial^2 T}{\partial x^2} \tag{2.7}$$

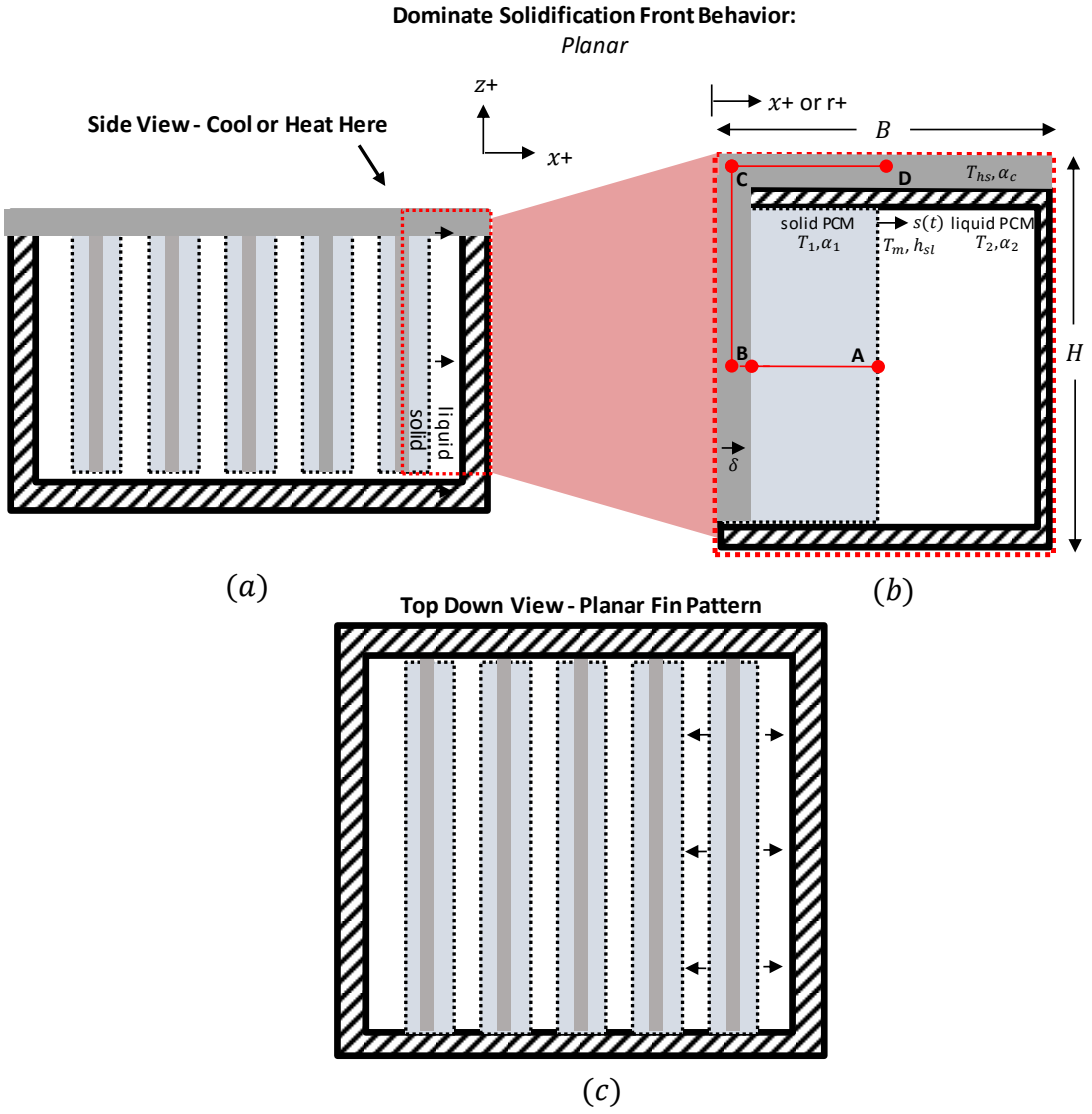

Figure 2.5 A PCM storage battery with planar fins interfacing with the PCM. The solidification process undergoes a planar dominated evolution of the solidification front. (a) and (c) show a side a top cross section view of the container, respectively. (b) shows the control volume at some time, $t > 0$, during the solidification process.

For solidification, the temperature at $x = 0$ is set to some value $T(t, z = 0) = T_0$, where $T_0 < T_m$ at $t \geq 0$. The following solution describes the evolution of the solidification process for $t > 0$. A solution for the temperature for two regions is needed. The first being the solidified region and second the liquid region. At the phase boundary the flux and temperature of the

liquid and solid phases are equal. The complete set of governing equations for the multiphase region is given in Equation (2.8).

$$\begin{cases} \dfrac{\partial x}{\partial t} = \alpha_1 \dfrac{\partial^2 T_1}{\partial x^2} & 0 < x < s(t)\,, \quad t > 0 \\ \dfrac{\partial x}{\partial t} = \alpha_2 \dfrac{\partial^2 T_1}{\partial x^2} & s(t) < x < \infty\,, \quad t > 0 \\ k_1 \dfrac{\partial T_1}{\partial x} + k_2 \dfrac{\partial T_2}{\partial x} = \rho h_{s\ell} \dfrac{ds}{dt} & x = s(t) \qquad t > 0 \\ BC's: \quad T(t,0) = T_0 \\ \qquad\qquad T\big(t, s(t)\big) = T_m \\ IC's: \quad T(0,x) = T_i \end{cases} \tag{2.8}$$

These equations can be re-written using dimensionless variables as in Equation (2.9).

$$\Theta = \frac{T_m - T}{T_m - T_0} \qquad \Theta_i = \frac{T_m - T_i}{T_m - T_0} \qquad X = \frac{x}{L} \qquad S = \frac{s}{L} \qquad \tau = \frac{\alpha_1 t}{L^2}$$
$$N_\alpha = \frac{\alpha_2}{\alpha_1} \qquad N_\kappa = \frac{\kappa_2}{\kappa_1} \qquad Ste = \frac{c_{p_1}(T_m - T_0)}{h_{s\ell}} \tag{2.9}$$

Where L is the thickness of the salt layer and is given by $\mathrm{L} = \mathrm{B} - \delta$ as shown in Figure 2.3. The detailed solution procedure is given in [29] and the result is repeated in Equation (2.10)

$$\theta(X,\tau) = \begin{cases} 1 - \dfrac{erf\left[\dfrac{X}{2\sqrt{\tau}}\right]}{erf[\lambda]} & X \le 2\lambda\sqrt{\tau} \\ \left(1 - \dfrac{erfc\left[\dfrac{X}{2\sqrt{N_\alpha \tau}}\right]}{erfc\left[\dfrac{\lambda}{\sqrt{N_\alpha}}\right]}\right)\theta_i & X > 2\lambda\sqrt{\tau} \end{cases} \tag{2.10}$$

Where λ is a constant given by Equation (2.11)

$$\frac{e^{-\lambda^2}}{erf(\lambda)} + \frac{N_k \theta_i}{N_\alpha^{1/2}} \frac{e^{-\lambda/N_\alpha}}{erfc(\lambda/N_\alpha^{1/2})} = \frac{Ste}{\lambda\sqrt{\pi}} \tag{2.11}$$

In the case of the Stefan problem, when $T_i = T_m$ it is clear that $\theta_i = 0$ and therefore Equation (2.11) simplifies to Equation (2.12).

$$\frac{e^{-\lambda^2}}{erf(\lambda)} = \frac{Ste}{\lambda\sqrt{\pi}} \tag{2.12}$$

Furthermore, in Equation (2.10) for values of $X > 2\lambda\sqrt{\tau}$ the temperature distribution is a constant value equal to T_m, the melting temperature of the PCM. It is worth noting that in the case of the Stefan problem the constant λ is a function that depends only on the Stefan number. That is, λ is dependent entirely on material properties and the thermal gradient in the control volume.

2.2.1.2 Cylindrical Dominated Solidification

Figure 2.6 depicts a phase change storage element that undergoes phase change with a cylindrically dominated phase change front. Depicted is a side cross section and top down view of cylindrical element along with a qualitative example of an alternate cylindrical fin pattern. The solution for fin pattern A will be considered. The solution procedure is identical

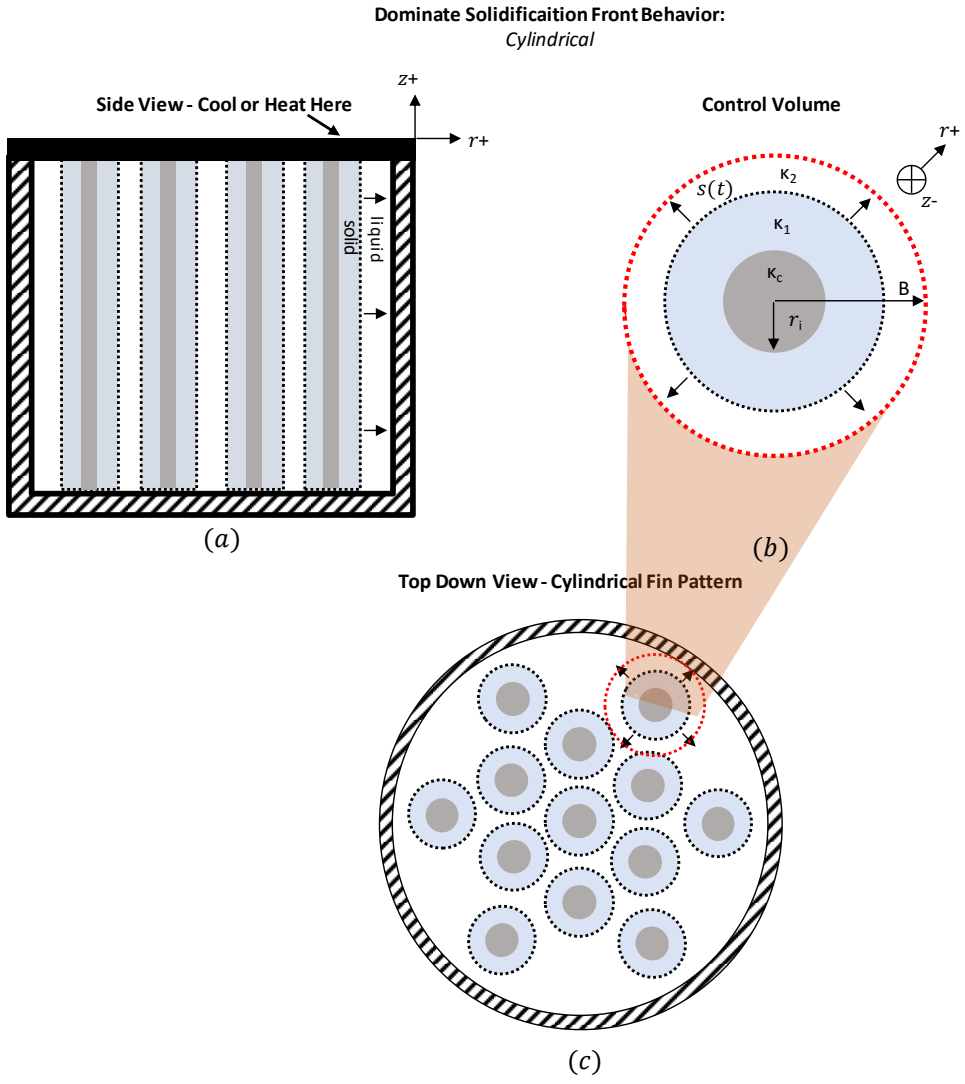

Figure 2.6 A PCM storage battery with cylindrical pin fins interfacing with the PCM. The solidification process undergoes a cylindrically dominated evolution of the solidification front. (a) and (c) show a side a top cross section view of the container, respectively. (b) shows the control volume at some time, t>0, during the solidification process.

to the solution for the planar case with the exception that the governing equations must be in cylindrical coordinates. Figure 2.2 and Figure 2.3 are applicable to this problem. The heat equation for a 1-D conduction controlled process in cylindrical coordinates is given in Equation (2.13)[30].

$$\frac{\partial T}{\partial t} = \alpha \frac{1}{r} \frac{\partial}{\partial r}\left(r \frac{\partial}{\partial r}\right) \tag{2.13}$$

Reference [31] gives multiple solutions under a variety of assumptions. The solution to the Stefan problem will be presented under a constant temperature inner boundary (Dirichlet boundary condition). The full set of governing equations is given in Equation (2.14).

$$\begin{cases} \dfrac{\partial T_1}{\partial t} = \alpha_1 \dfrac{1}{r} \dfrac{\partial}{\partial r}\left(r \dfrac{\partial T_1}{\partial r}\right) & r_i < r < s(t)\,, \quad t > 0 \\ k_1 \dfrac{\partial T_1}{\partial r} = \rho_1 \mathrm{h}_{s\ell} \dfrac{ds}{dt} & r = s(t) \quad t > 0 \\ BC's: \quad T(t, r_i) = T_0 & t > 0 \\ \quad T\big(t, s(t)\big) = T_m & \\ IC: \ T(0, \mathrm{r}) = T_m & \end{cases} \tag{2.14}$$

Using the dimensionless variables defined in Equation (2.15).

$$\Theta = \frac{T_m - T}{T_m - T_0} \qquad R = \frac{r}{\delta} \qquad S = \frac{s}{\delta}$$
$$\tau = \frac{\alpha_1 t}{\delta^2} \qquad Ste = \frac{c_{p_1}(T_m - T_0)}{\mathrm{h}_{s\ell}} \tag{2.15}$$

The temperature distribution is described by Equation (2.16).

$$\theta(X,\tau) = \begin{cases} -\dfrac{(\phi+1)log^2(R)}{log^2(S)} + \dfrac{\phi\, log(R)}{log(S)} + 1 & R \le S(\tau) \\ 0 & R > S(\tau) \end{cases} \tag{2.16}$$

Where $\phi = (\sqrt{2Ste+1}-1)/Ste - 2$ and S is the position of the phase change front determined by a numerical solution to Equation (2.17).

$$\frac{1}{4}(1-S^2) + \frac{1}{2}S^2\, log(S) - \left(\sqrt{2Ste+1}-1\right)\tau = 0 \tag{2.17}$$

The solutions presented here can be used to inspect how geometric and thermophysical parameters affect the solidification process.

2.2.2 Numerical Solutions

Equations (2.12) and (2.17) do not have closed form solutions and therefore must be solved numerically for the constant λ, and S, respectively. The numerical solutions to these constants can then be plugged into Equations (2.10) and (2.16) to recover the temperature distribution in the multiphase region. Wolfram Mathematica 10.0 was used to calculate the numerical solutions with the material properties of $NaNO_3 - KNO_3$ Eutectic (52: 48) in Table 2.1. The Mathematica code to reproduce the solutions is contained in Appendix B. In all analytical solutions the boundary condition is a dirichlet boundary with a temperature, T_0, that was set to a minimum allowed cooking temperature of $T_{min} = 180\ °C$. T_{min} was determined from the assumption of a nominal cooking temperature of 200 $°C$ and allowable variation of 20 $°C$ below the nominal value such that $T_0 = T_{min} = T_{nominal} - T_{allowable} = 180\ °C$. A boundary temperature of 180 $°C$ will give insight into the heating rates expected

when a cooking surface falls to an estimated minimum functional temperature for a high heat setting.

2.2.2.1 Planar Solidification

Calculating the temperature distribution in the solidifying Solar Salt PCM layer over time in dimensional coordinates is valuable to gain understanding of the phase change process in a STEC that is a practical size for rural communities. For this reason, the dimensional solution to Equation (2.10), is plotted in Figure 2.7. Due to the dirichlet boundary condition the thermal gradient between the progressing solidification front and the PCM to planar fin

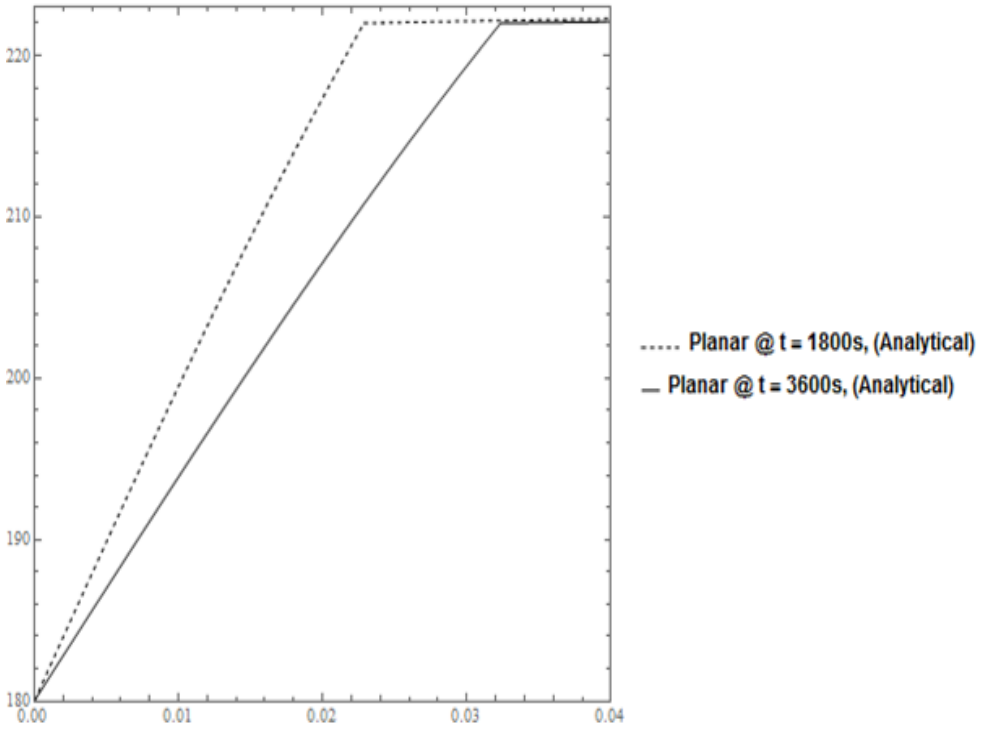

Figure 2.7 Temperature distribution as a function of PCM layer depth in a Planar dominated solidification front with $T(t > 0, x = 0) = T_0 = 180$ ℃ at $t = 1800s$ and $t = 3600s$. Note that since the boundary at $T(t, x = 0)$ is constant ΔT_{AB} is a constant value of 42℃.

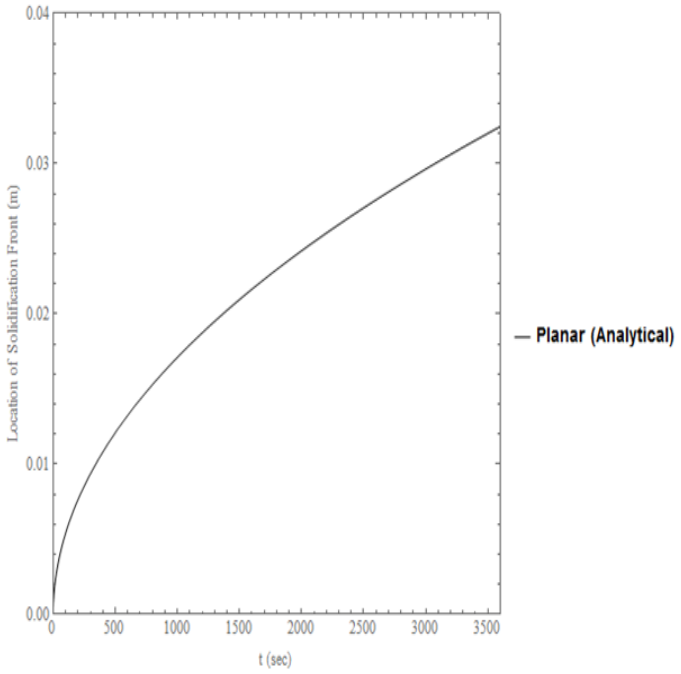

Figure 2.8 Location of the solidification front over time in planar dominated solidification. At $t = 3600s$ the solid layer of PCM has thickness of 0.0325 m or 3.25 cm.

interface is constant. Since flux, determined by Equation (2.5), is proportional to dT/dx, Figure 2.7 illustrates flux decreasing over time within the solid PCM layer. The non-linear behavior of the planar solidification process is also apparent when solving for the location of the solidification front with respect to time, shown in Figure 2.8, and flux as a function of position in the solid PCM layer thickness at $t = 1800s$ and $t = 3600s$, shown in Figure 2.9. Notice that the speed of the melt front, ds/dt, is decreasing over time due to the decreasing flux in the solid PCM layer (Figure 2.8). On the PCM to planar fin interface ($x = 0\ m$) the flux drops 29% from 1582 W/m^2 at $t = 1800s$ to 1119 W/m^2 at $t = 3600s$. The decline in flux extracted from the PCM at the PCM to planar fin interface ($x = 0\ m$) is not linear, as illustrated in Figure 2.10, the flux at the planar fin interface drops rapidly at the start of solidification and is relatively stable during the times plotted in Figure 2.9.

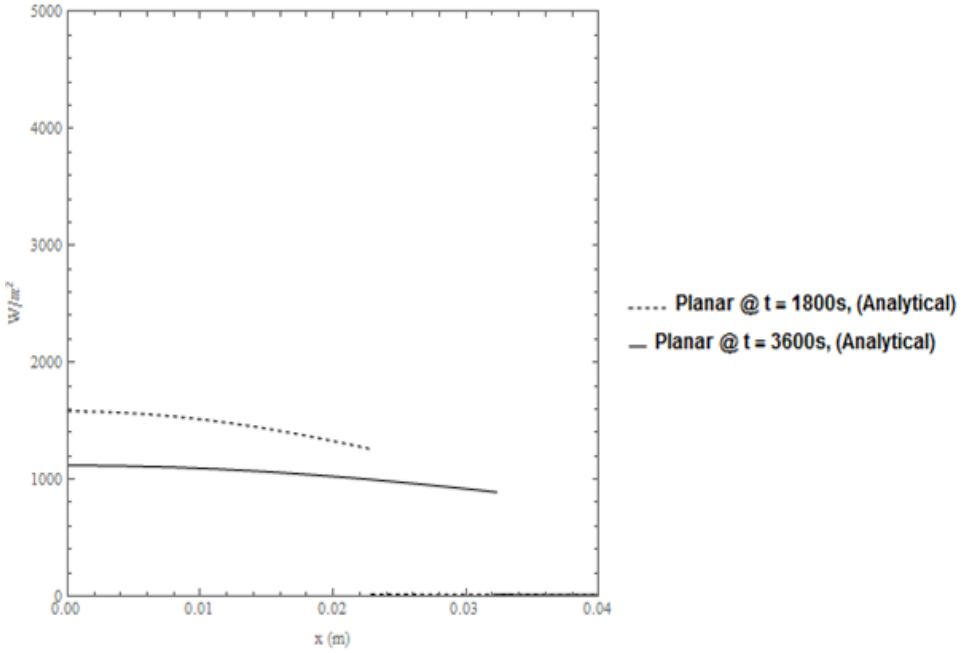

Figure 2.9 Comparison of the flux as a function of solid PCM layer thickness at $t = 1800s$ and $t = 3600s$ for a planar dominated solidification front. The flux drops to zero sharply at the solid to liquid phase boundary.

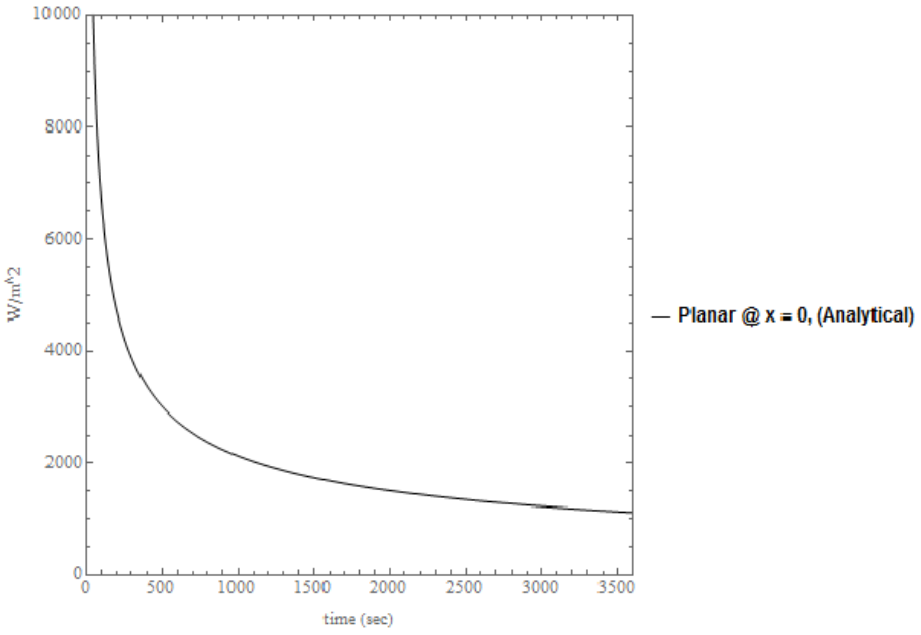

Figure 2.10 Flux over time on the PCM to planar fin interface ($x = 0\ m$) with $T(t, 0) = T_0 =$ 180 ℃. Flux drops 29% from 1582 W/m^2 at $t = 1800s$ to 1119 W/m^2 at $t = 3600s$.

2.2.2.2 Cylindrical Solidification

The charts generated for the planar case show expected flux under a constant temperature boundary if planar fins are used. For comparison the dimensional solution to the case of cylindrical pin fins, Equation (2.14), was solved in the same manner with the same boundary condition and at the same times as the planar case. Figure 2.11 shows the temperature distribution as a function of depth within the solidifying cylindrical PCM layer as a function of PCM layer thickness. An important difference in the cylindrical case over the planar case is a need to define an initial radius for the pin fin and solidifying PCM. The initial radius used in all cylindrical solutions is $r_i = 0.25\,in = 0.00635\,m$. An inner radius of $0.00635\ m$ matches the inner pin radius of an experiment performed on a pin fin array which is detailed in *Chapter 3:Experimental Apparatus*. Figure 2.12 shows flux as a function of PCM layer thickness and Figure 2.13 shows flux as a function of time at $r = r_i$.

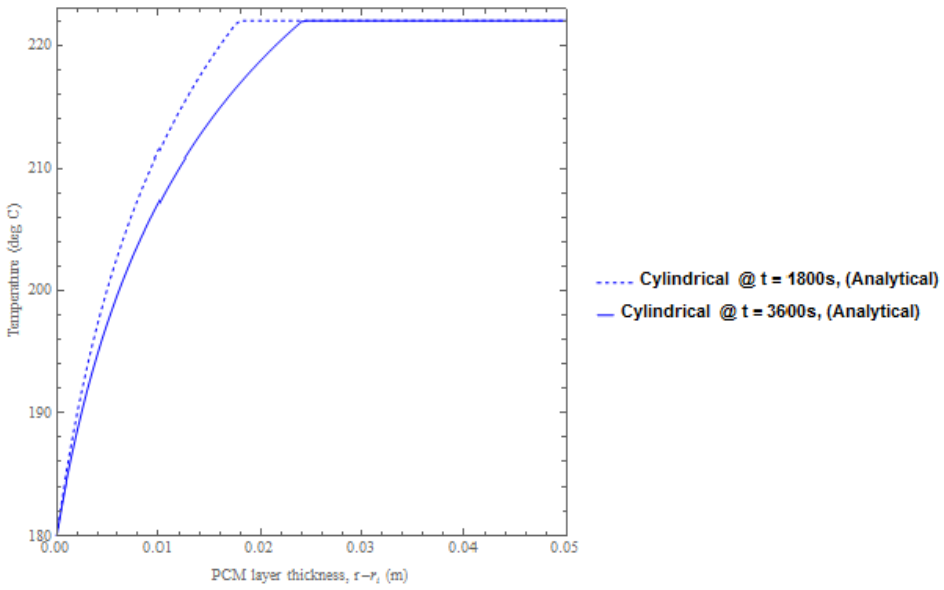

Figure 2.11 Temperature as a function of PCM layer thickness within a cylindrically dominated solidification front with $T(t > 0, r = ri) = T_0 = 180$ ℃ at $t = 1800s$ and $t = 3600s$. The boundary at $T(t, r = r_i = 0.00635\,m)$ is constant so ΔT_{AB} is constant at 42℃. The solid layer of PCM has a thickness of 2.4 cm at $t = 3600s$.

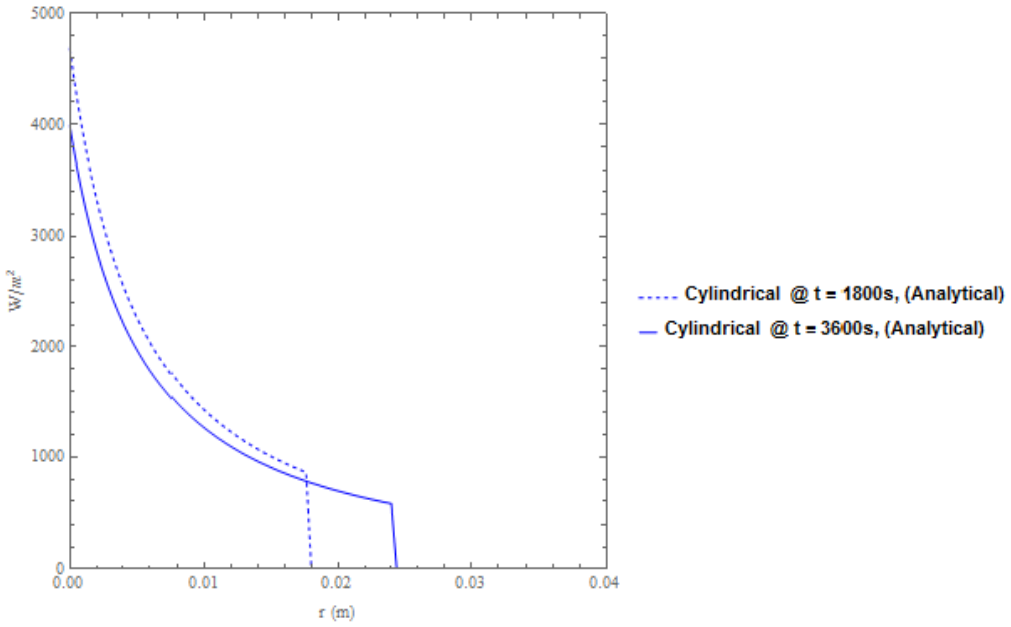

Figure 2.12 Comparison of flux as a function of PCM layer thickness within a cylindrically dominated solidification front $T(t > 0, r = ri) = T_0 = 180$ ℃. Note how the flux drops to zero sharply at the solid to liquid phase boundary.

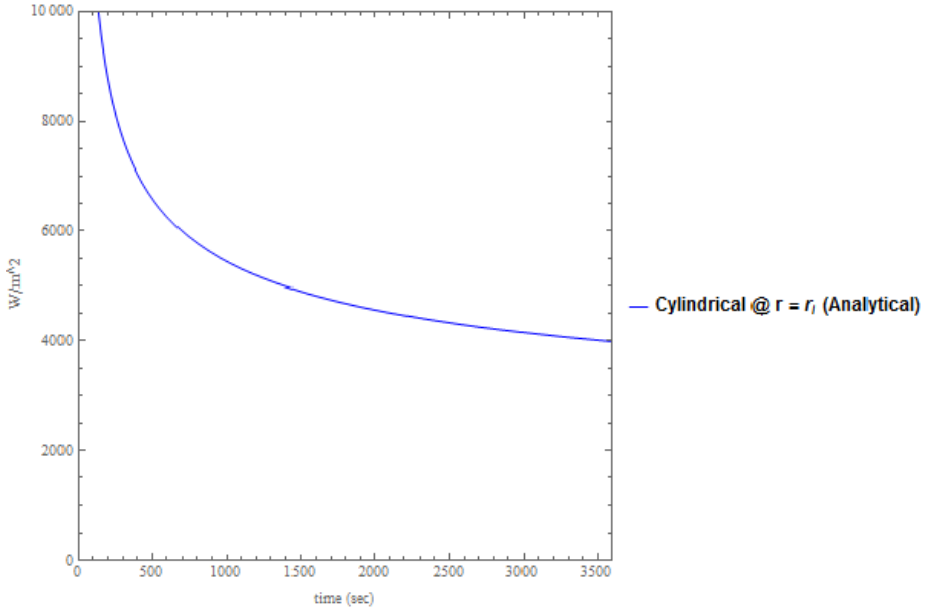

Figure 2.13 Flux over time on the PCM to cylindrical pin fin interface ($r = ri = 0.00635\ m$) with $T(t > 0, r = r_i) = T_0 = 180$ ℃. Flux drops 15% from 4684 W/m^2 at $t = 1800s$ to 3986 W/m^2 at $t = 3600s$.

2.2.2.3 Comparison of Planar to Cylindrical

Comparing the analytical solutions of planar and cylindrically dominated solidification yields insights into how geometry affects solidification and flux stability. The temperature distribution as a function of PCM layer thickness for planar and cylindrical solidification at $t = 1800s$ and $t = 3600s$ with $T_0 = 180$ °C is compared in Figure 2.14. Figure 2.15 compares the flux as a function of PCM layer thickness at the same times and under the same conditions and Figure 2.16 compares the flux over time at the fin to PCM interface. The illustrations show that the liquid to solid phase boundary advances more quickly in the planar case, having a solid PCM thickness of 3.3 cm versus 2.4 cm in the cylindrical case after 3600s. Furthermore, the flux at the pin to PCM interface is higher and more stable in the cylindrical case dropping only 15% from 4684 W/m^2 at $t = 1800s$ to 3986 W/m^2 at $t = 3600s$ versus a drop of 29% from 1582 W/m^2 at $t = 1800s$ to 1119 W/m^2 at $t = 3600s$.

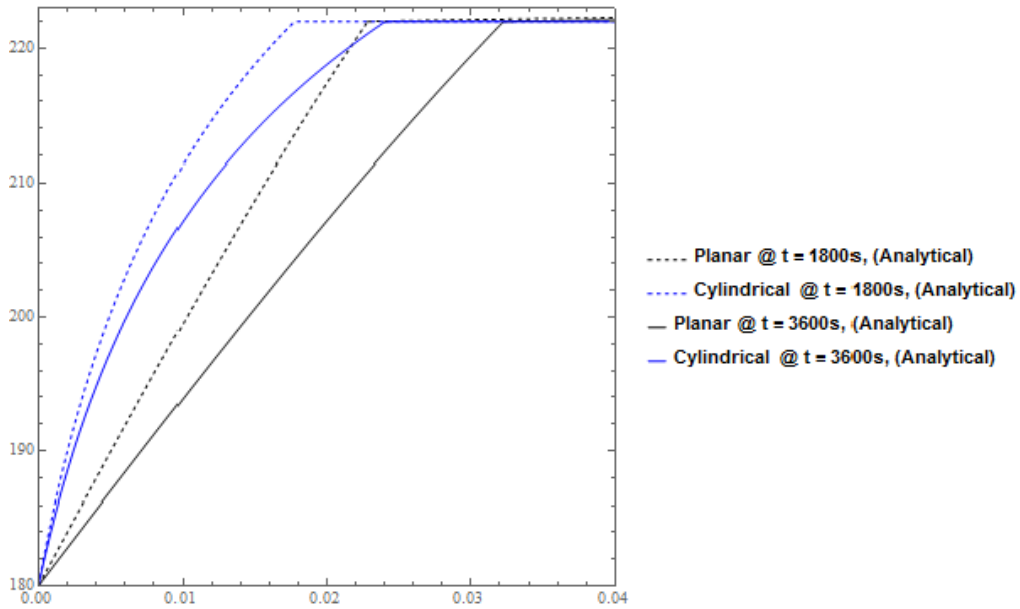

Figure 2.14 Temperature vs solid PCM layer thickness for a Planar or Cylindrically dominated solidification front with $T(t > 0, PCM\ thickness = 0) = T_0 = 180$°C at $t = 1800s$ and $t = 3600s$. The solid to liquid phase boundary advances to 3.3 cm in the planar case versus 2.4 cm in the cylindrical case after 3600s.

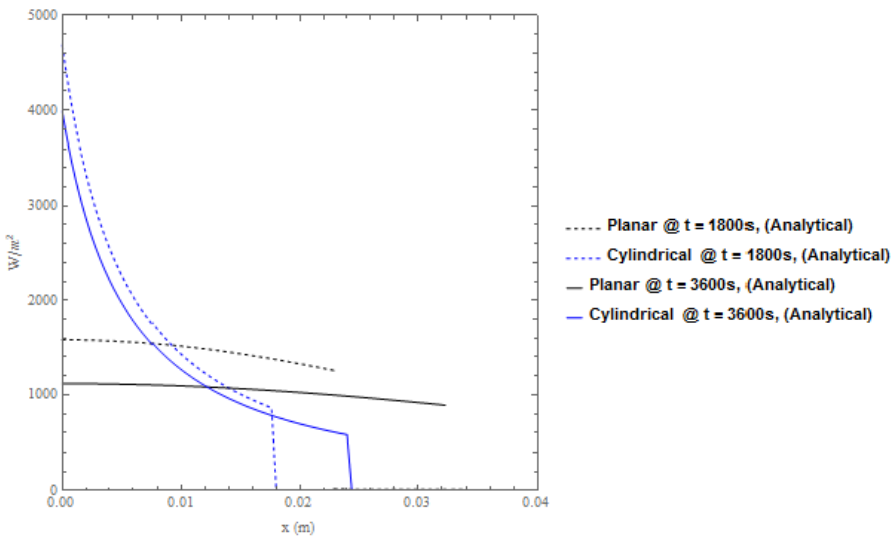

Figure 2.15 Flux vs solid PCM layer thickness for a Planar or Cylindrically dominated solidification front with $T(t > 0, PCM\ thickness = 0) = T_0 = 180$ ℃ at $t = 1800s$ and $t = 3600s$. In the cylindrical case flux drops 15% from 4684 W/m^2 to 3986 W/m^2 versus a drop of 29% from 1582 W/m^2 to 1119 W/m^2 in the planar case.

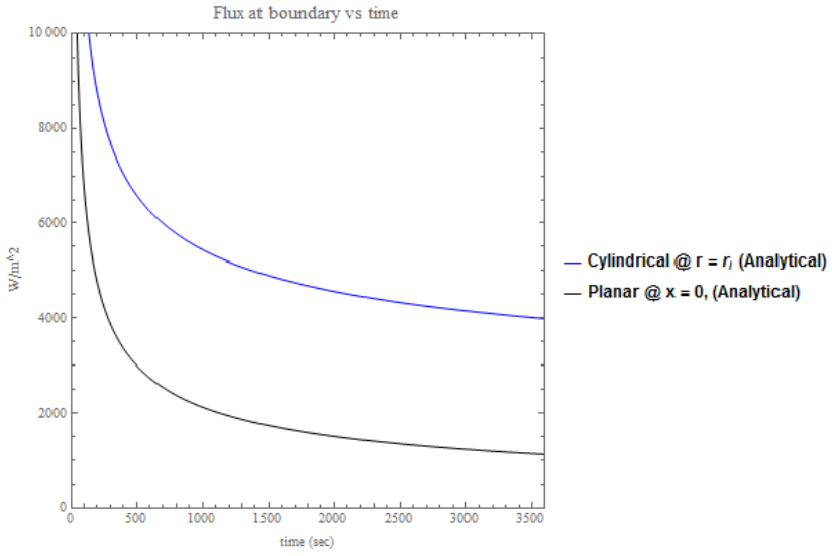

Figure 2.16 Flux versus time at the fin to PCM interface with a Planar or Cylindrically dominated solidification front with $T(t > 0, PCM\ thickness = 0) = T_0 = 180$ ℃

Comparing the dirichlet solution of 1-D cylindrical and planar solidification aids in understanding that flux varies greatly during solidification in region AB in Figure 2.3, and that the variation is greater in the case of planar solidification. Understanding the entire gradient ΔT_{ABCD} in more detail requires coupling the multiphase solution with the solid conduction solution of the fin array. Furthermore, to model cooking a dirichlet boundary condition is not appropriate. During a cooking session flux and temperature of the surface will change as the temperature of the food changes, among many other factors. The complete thermal gradients of a real container, including gradients in the pin element, can be aided considerably utilizing Finite Element Modeling (FEM). The analytical solutions will be used to verify the accuracy of the FEM results.

2.3 ANSYS FEM Multiphase Heat Transfer Models

An idealized Finite Element Model (FEM) of the multiphase solidification process was generated for planar and cylindrical cases. Because addition of a heat spreader and fin array will cause the solidification process to deviate from its 1-D idealized form, a simplified baseline FEM model was first generated (Figure 2.17) to confirm accuracy of the FEM model relative to the analytical solutions. After correlation of the analytical solutions to and idealized FEM model a cylindrical fin and heat spreader will then be added. The material properties of the PCM are $NaNO_3 - KNO_3$ Eutectic (52: 48) in Table 2.1 and were input as an enthalpy within an ANSYS non-linear transient thermal analysis module. Enthalpy was input as a temperature dependent term with the rapid change of enthalpy at the phase

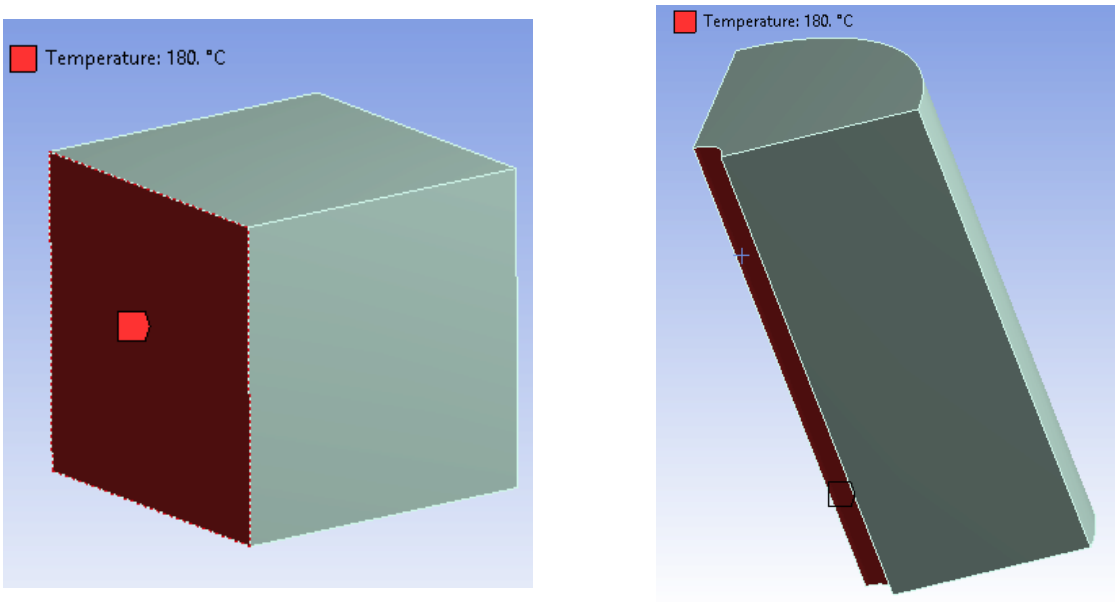

(a) Planar Solid (b) Cylindrical Solid

Figure 2.17 (a) A planar cube of Solar Salt PCM with the boundary $T(t > 0, PCM\ thickness = 0) = T_0 = 180$ °C indication in red (b) A Cylindrical solid of the same material with the boundary $T(t > 0, PCM\ thickness = 0) = T_0 = 180$ °C indicated in red.

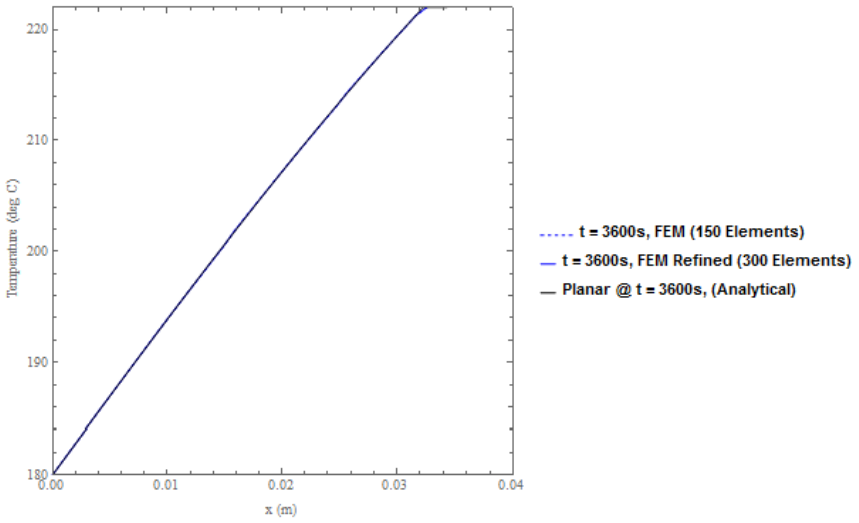

(a)

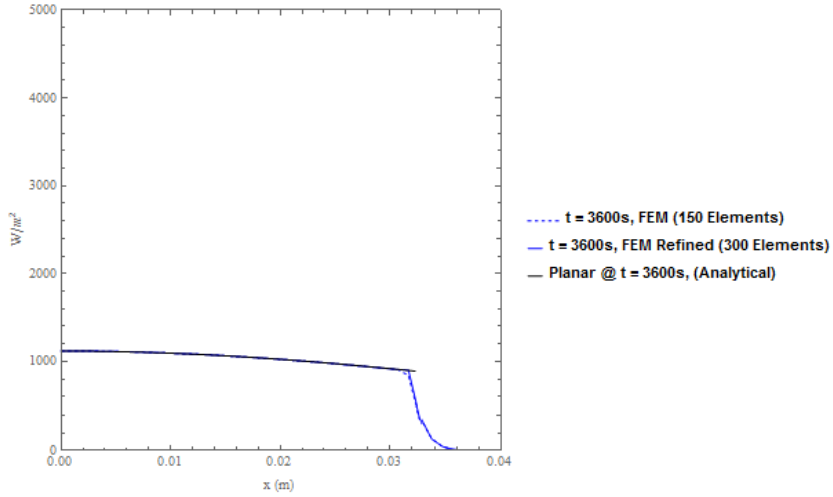

(b)

Figure 2.18 (a) Temperature vs Solid PCM layer thickness for Planar solidification with $T(t > 0, PCM\ thickness = 0) = T_0 = 180$°C with 150 Elements vs 300 elements compared to analytical solution (b) Flux vs Solid PCM layer thickness for Planar solidification with $T(t > 0, PCM\ thickness = 0) = T_0 = 180$°C with 150 Elements vs 300 elements compared to analytical solution. Noticeable differences between the FEM model analytical solution only exist at the solid to liquid phase boundary.

boundary added over a 1 °C temperature range centered at the Solar Salt melting point. The details of how the enthalpy was calculated is contained in Appendix B. Comparison was made first to the planar model with varying mesh refinement to confirm convergence. Figure 2.18 shows the result of comparing the planar model with 300 elements in the direction of

solidification vs 150 elements. Deviation from the analytical solution only exists at the phase boundary and further reduction in the size of the mesh yielded a transient solution that did not converge. Correlation of the cylindrical idealized case to the 1-D analytical cylindrical solution is contained in Appendix B.

2.3.1 FEM model with Cylindrical Pin Fin Array

A 3-D FEM model of a cylindrical pin fin imbedded in the PCM was developed to explore 2-D gradients within a simplified element of solidifying PCM that simulates the action of cooking on a heat spreading surface connected to the pin fin(s). A cross section through a 90-degree arc of the cylindrical model is shown in Figure 2.19. The model is intended to simulated the simplified element shown previously in Figure 2.3 with all boundaries of the PCM adiabatic

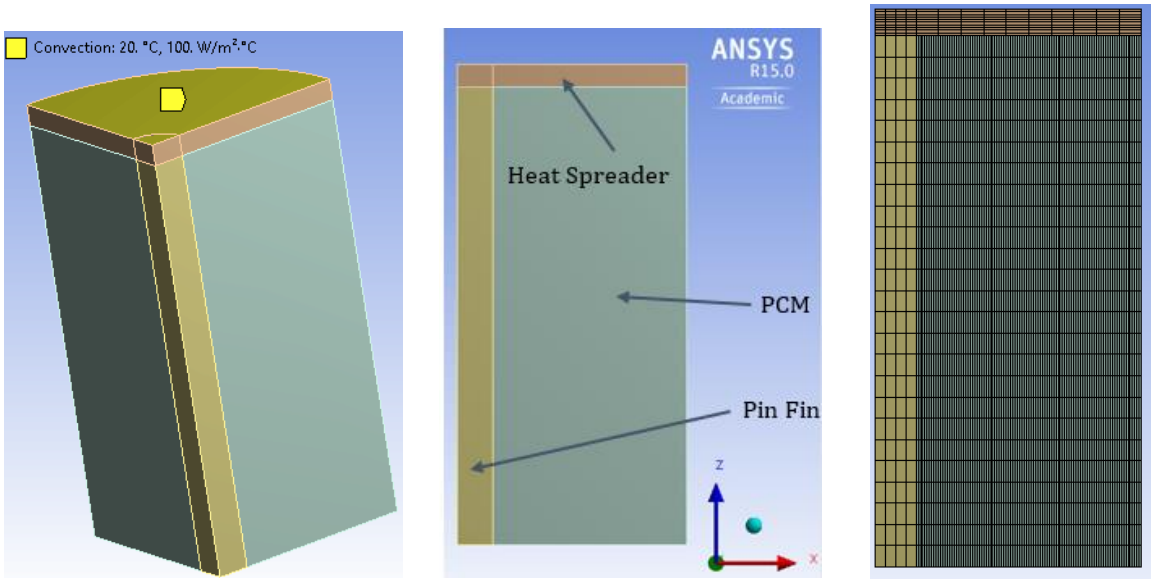

(a) (b) (c)

Figure 2.19 (a) View of the 90-degree arc of the cylindrical model shown with the convection boundary of 100 W/m^2 at 20°C. All solid bodies have an initial temperature of $T_0 = 222.5$°C. (b) Front view of the ANSYS solid bodies in the transient thermal model, the heat spreader and pin fin are modeled as 6061 Aluminum(c) finite element mesh with 32,215 elements and 143,556 nodes. The higher density mesh was required to achieve convergence under high thermal fluxes.

except the heat spreading surface. The thermal model also matches the dimensions of the experimental apparatus detailed in Chapter 3. The PCM is bonded to the pin fin, no thermal interface in included in the model between the pin fin and the PCM. The boundary on the +z side of the heat spreader, shown in Figure 2.19 (a), was set to a convective boundary of 100 W/m^2 at 20°C to simulate the effect of cooking on the heat spreader. The radius of the pin fin is $r_i = 0.25\ in = 0.00635\ m$ and the outer radius of the element extends to $r_0 = 0.05\ m$ with a pin length of 0.0836 m. The ratio of PCM layer outer radius to the pin fin length is intentionally chosen to be large to highlight the impact of thermal gradients with the pin fin on the evolution of the phase change boundary. Due the pin fin temperature gradients,

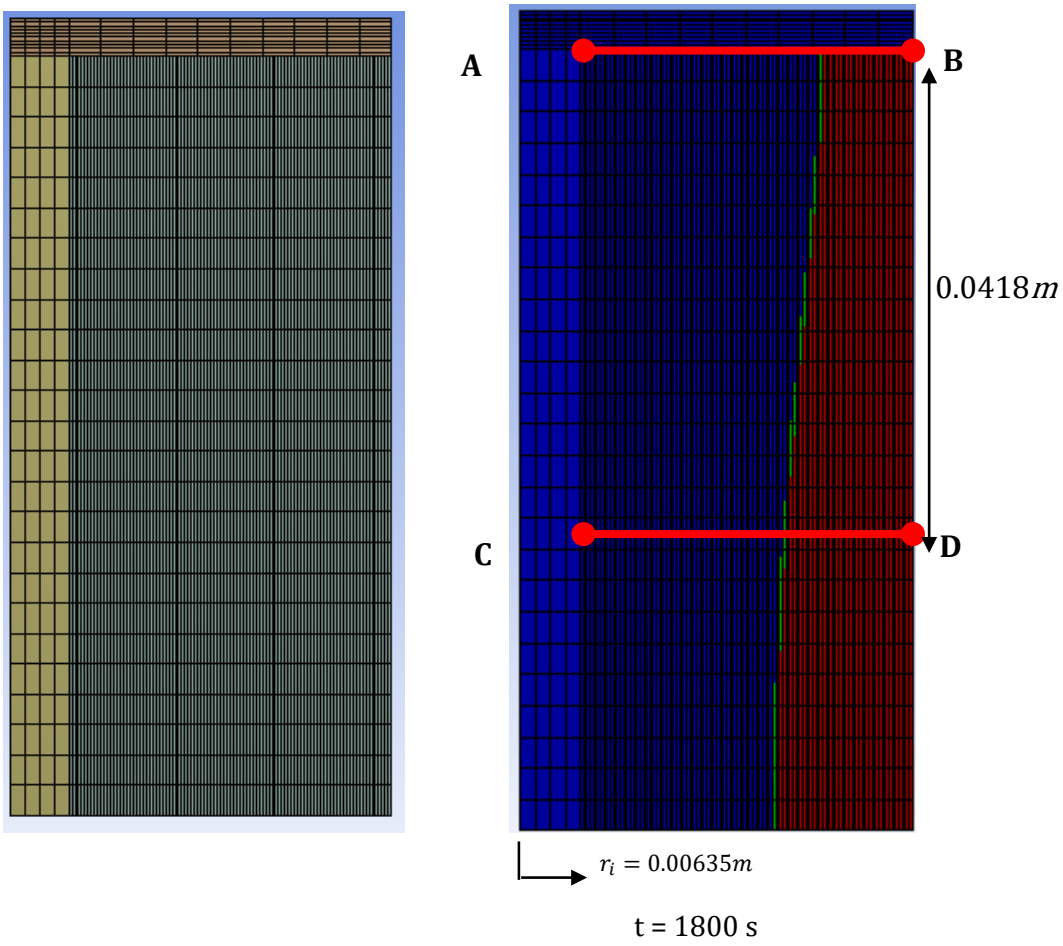

Figure 2.20 Close up of cylindrically dominated phase change process. The numerical temperature profiles of lines AB and CD can be compared to the analytical solution.

the solidification front within the PCM develops a curved shape as shown in Figure 2.21. Ideally, the phase change front will remain parallel to the vertical axis of the pin during the entire time of discharging heat. When the phase change boundary nearest the heat spreader reaches the outer boundary the phase change process ends and the flux and temperature of the heat spreader will drop more rapidly at that time. The temperature of the PCM will also begin to drop rapidly, and before the phase change process has fully completed. These effects are an additional source of thermal gradients that contribute to the value of $\eta < 1$(Equation (2.2)). Comparing the impact of incorporating the fin array on solidification can be done by comparing the pin fin model to the analytical solution.

Figure 2.20 shows an enlarged view of the ANSYS results at $t = 1800\ s$. Lines AB and CD will be used for comparison locations to the analytical solution. Recall the 1-D analytical solution only requires a single boundary temperature to reconstruct the temperature gradient with the PCM, assuming the boundary is constant. Since the boundary from the Pin FEM model is

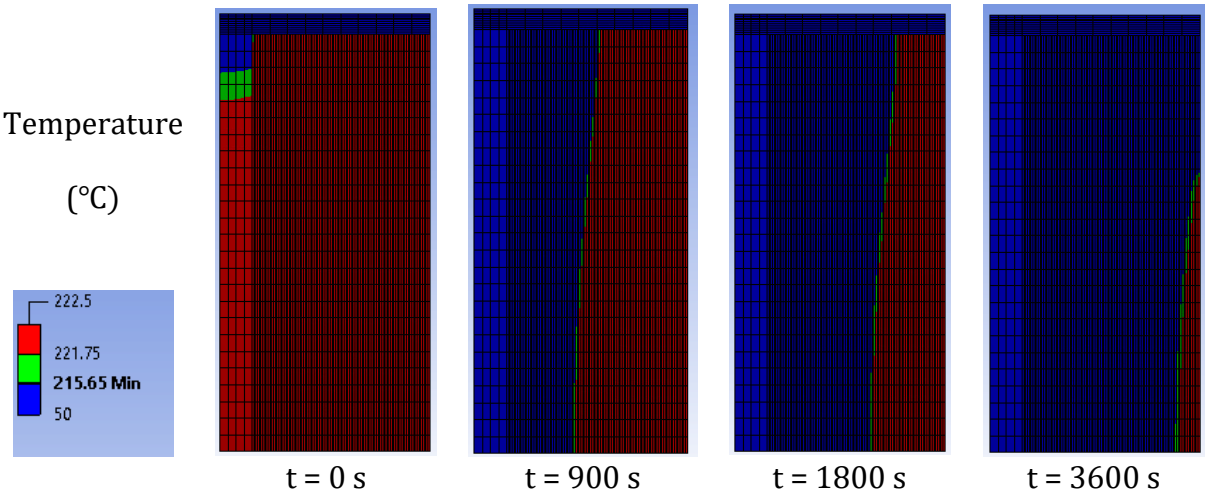

Figure 2.21 Phase change front evolution for a cylindrically dominated phase change process. Blue indicates solid PCM, red liquid PCM, and green indicates the phase boundary.

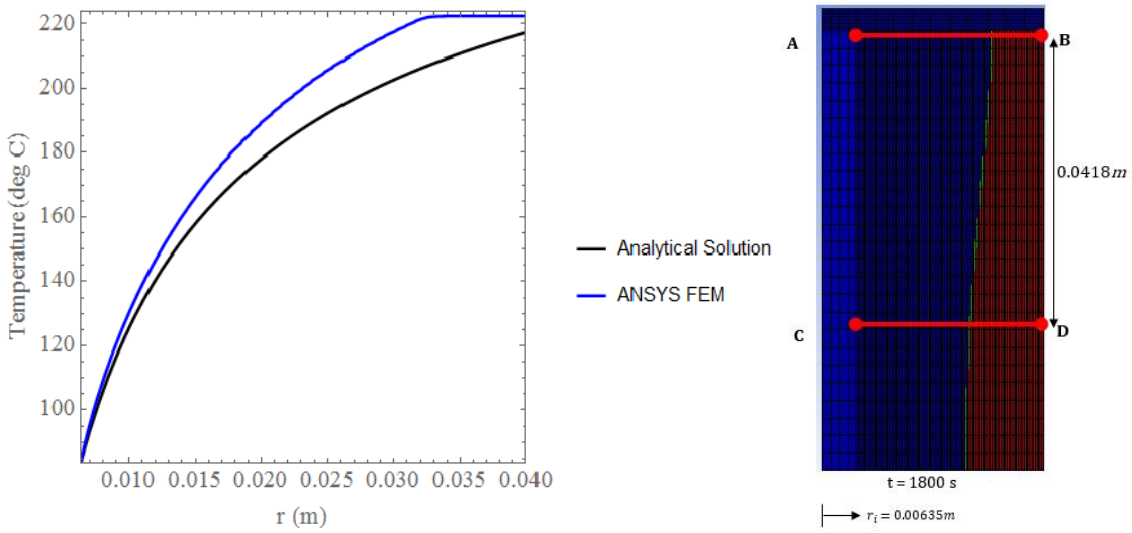

Figure 2.22 Comparison of the analytical solution of a cylindrical pin fin to the ANSYS thermal model along line AB at t = 1800s. The boundary condition in the analytical solution is $T_0 = 84$ °C, which is the ANSYS result for the salt to pin boundary temperature at point A.

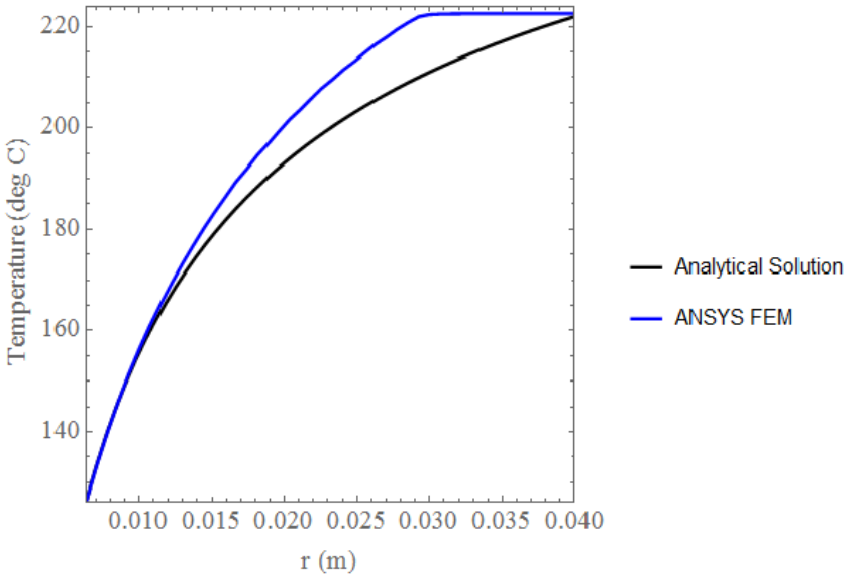

Figure 2.23 Comparison of the analytical solution of a cylindrical pin fin to the ANSYS thermal model along line CD at t = 1800s. The boundary condition in the analytical solution is set $T_0 = 126$ °C, which is the ANSYS result for the salt to pin boundary temperature at point C.

convective and not a constant temperature or constant flux the expectation will be deviation from the idealized 1-D analytical solidification model. The temperature profile for line AB is

shown in Figure 2.22 and the temperature profile for line CD is shown in Figure 2.23. The location of the solidification front is indicated by the sharp discontinuity in the FEM curves once the temperature reaches the melt temperature. The impact of the pin fin is clear, the solidification front of the analytical 1-D case has completed in the cavity illustrated in Figure 2.22 and Figure 2.23 while the FEM solidification process is ongoing.

While the location of the phase change front is noticeably slowed in the FEM model, the temperature profiles are remarkably similar. Deviation from the ideal analytical solution is expected. Since there is an aluminum pin element included in the FEM model, the added thermal mass and thermal resistance of the pin element is expected to slow the solidification process. In the design of a real thermal energy storage device, such effects are important to consider, since they will have an impact on the temperature and fluxes within the device. The advantage of a finite element model comes from the ease of incorporating non-ideal effects including increased thermal mass from fin arrays embedded in the PCM, heat leak from the insulation container outside of the PCM, manufacturable fin geometries, etc.

2.3.2 FEM Model Cooling Rate Results

From the FEM model estimates for the value of ΔT_{ABCD} can be determined under a boundary condition that more realistically models cooking. Referring again to Figure 2.20 the heat spreader cooled from an initial temperature of 222 ℃ to 75 ℃, a ΔT_{ABCD} of 147 ℃, after 30 min (1800s). That is a linear average cooling rate of approximately 5 ℃/min with the cooling rate being considerably more rapid at the start of PCM solidification. Shown in Figure 2.24 is a plot of temperature at the cooking surface over time for the FEM model with a convective

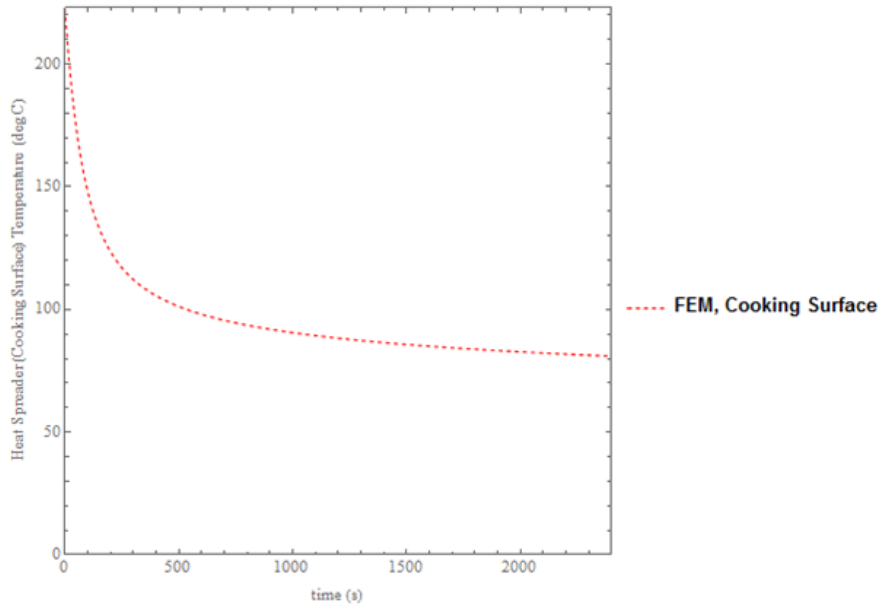

Figure 2.24 ANSYS model cooking surface temperature over time with a convective boundary of 100 W/m^2 at 20℃ . The cooking surface falls under the 180 ℃ min cooking surface temperature at $t = 43s$.

boundary condition. The cooking surface falls under the 180 ℃ min cooking surface temperature at $t = 43s$. Figure 2.25 illustrates the heat extracted from the pin fin model depicted in Figure 2.19.

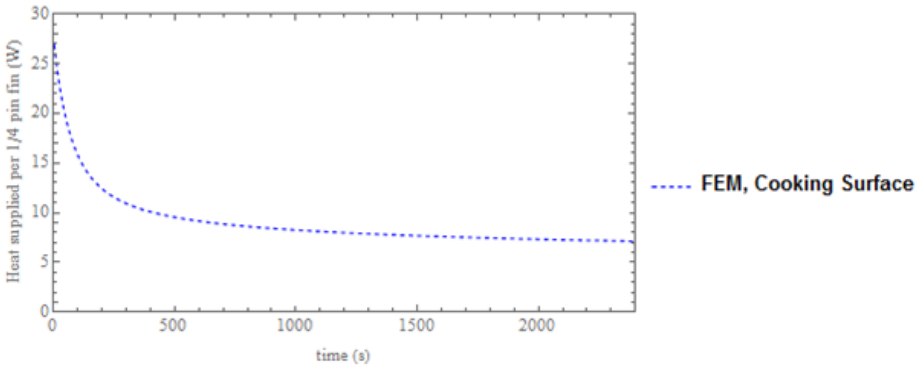

Figure 2.25 Heat extracted from the convective boundary vs time. The heat rate drops to 40W per pin from a value an initial value of 100W per pin.

Chapter 3: Experimental Apparatus

3.1 Construction of 3rd Generation STEC

The 3rd Generation of STEC had the dual purpose of being a small demonstration of a Stored Energy Solar Cookstove as well as a modular apparatus for performing a water boiling experiment. The PCM utilized in the experiment was $NaNO_3 - KNO_3$ Eutectic (52: 48) "Solar Salt" with the material properties listed in Table 2.1. A vessel was constructed of 6061 Aluminum and four 4.5" long, ½" diameter rods were braised into 1/8" deep holes in a 4" x 1/4" circular heat spreader of the same material. The pin fin array was inserted into a capped cylinder and the seam was brazed as shown in Figure 3.1. The hollow cylinder was filled with 0.6 L of liquid Solar Salt and the cylinder was inserted into an Isosteel 1.5L 18/8 Stainless Steel Vacuum insulated food container. The vacuum thermos provided an effective approximation of an adiabatic outer boundary. An air gap between the surface of the PCM

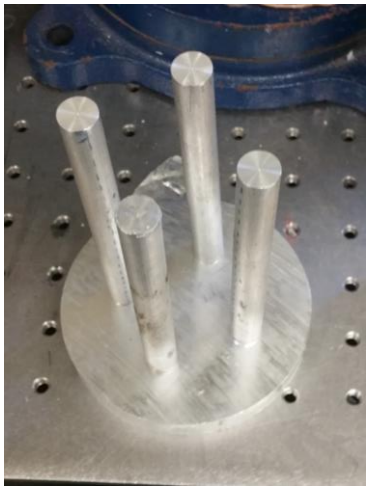

(a)

(b)

Figure 3.1 (a)Assembled aluminum 6061 pin fin array and (b) the fully assembled heat spreader pin fin array and cylindrical vessel.

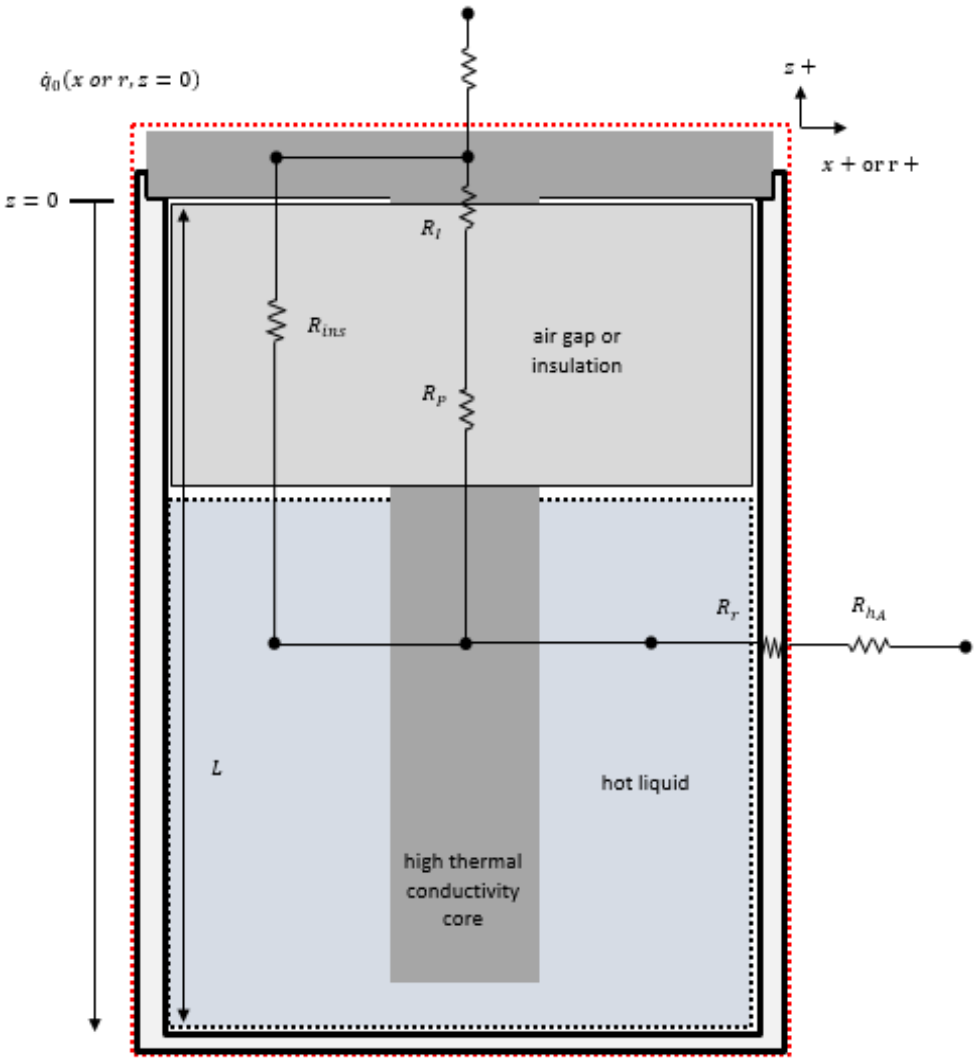

Figure 3.2 Thermal circuit of the experimental set-up. The high thermal conductivity core (pin fin) is designed as the dominant heat path from the PCM to the environment.

and the heat spreader provided insulation at that interface. A thermal circuit of a simple single pin apparatus is shown in Figure 3.2. The thermal circuit for the 3rd Generation of STEC is the same except four small pins were used instead of a single large pin. The prototype was built such that the dominant heat path is through the pin element(s). To provide a low temperature thermal sink and simulate a common cooking activity a pot of 0.5 L of water was placed on top of the heat spreading surface. Avocado oil was used as a thermal interface oil with the pot to reduce the thermal gradient between the base of the pot and heat spreader.

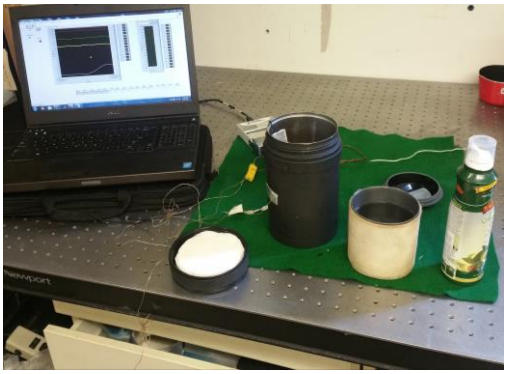

(a)

(b)

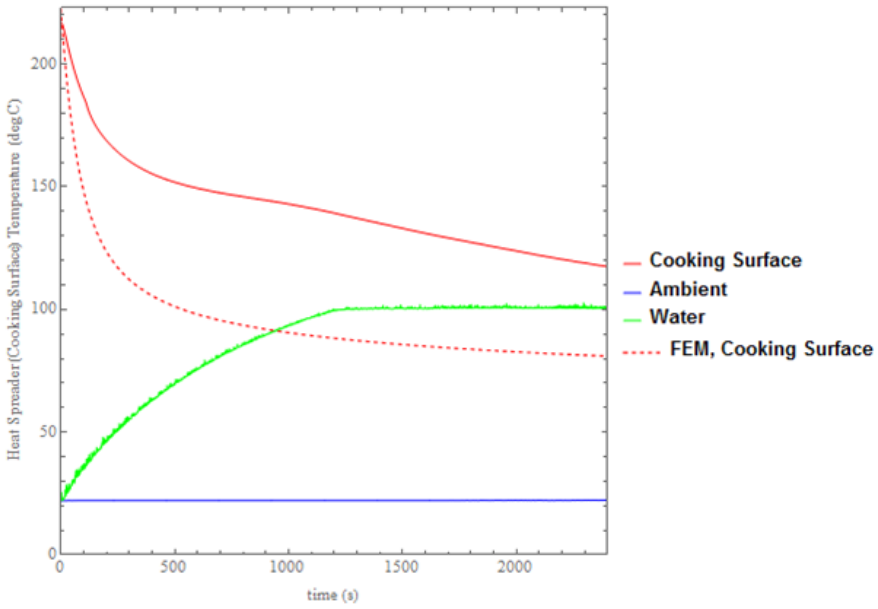

(c)

Figure 3.3 (a) Equipment used in water boiling experiment from top left to right - laptop running LabVIEW, Isosteel Vacuum thermos and Lid, water and pot, avocado oil spray. (b) a Thermo Scientific oven and (c) temperature over time results. The cooking surface temperature of the FEM model is shown for comparison.

Avocado oil was selected for its high smoke point of 271 °C. Six Type-K thermocouples were used to take internal and external temperature measurements. LabVIEW was utilized for data acquisition along with a National Instruments thermocouple data logger.

The vessel with the phase change material was heated in a Thermo Scientific oven to melt the Solar Salt and soaked for roughly four hours to insure a uniform initial temperature in the liquid PCM. The equipment used and the results from the experiment are shown in Figure 3.3. It took 20 min to bring the water to a boil and the water then simmered for 22 minutes. The average flux on the cooking surface was 21,000 W/m^2 over the time it took the water to boil. The flux on the pin to PCM interface is scaled simply by the area ratio between the surface area of the pins and the area of the cooking surface. For the 3rd Generation of STEC the cooking surface to pin area ratio is 0.47 which gives an average pin surface flux of approximately 10,000 W/m^2 on average.

3.1.1 Water Boiling Experiment Cooling Rate Results

During the water boiling experiment, the temperature of the cooking surface dropped from 216 ℃ to 140 ℃, a ΔT_{ABCD} of 76 ℃, after 20 min (1600s). That is a linear average cooling rate of approximately 3.8 ℃/min, lower than the PCM cooking surface linear cooling rate of 5 ℃/min, suggesting the convective boundary of the ANSYS FEM model is high as an analogue to cooking. At the 3.8 ℃/min cooling rate from the water boiling experiment the cooking surface drops below 180 ℃ in 11 min. These illustrations show clearly that the temperature of the cooking surface in STEC drops rapidly during discharge, due to temperature gradients that arise in the phase change material and interfacing array of fins.

Chapter 4: Discussion and Recommendations

The goal of this thesis was to match the heat flux requirements of cooking using thermal energy stored in a eutectic mixture of $NaNO_3 - KNO_3$, recommend a conceptual design of STEC that balances thermal performance with observations of user needs, and identify any remaining obstacles to the widespread adoption of STEC (Section 1.1.4). To accomplish these goals an analysis and test was performed to determine the fundamental limitations of storing and extracting heat from a PCM at high flux, specifically with regards to temperature and flux stability during discharge (cooking) of the Stored Thermal Energy Cookstove.

An estimation of required heating rates and temperatures for common cooking activities was performed which, combined with a combination of field observations of villages in India and laboratory testing, determined that to providing reasonable cooking performance requires maintaining a temperature of 200 °C without falling below 180 °C during the period of cooking. The Analytical and FEM analysis indicate flux stability is at best 15% stable in an idealized case during the final 30 min of a 1-hour cooking session with a cylindrically dominated melt front. Experimental results indicate a linear average cooling rate of around 3.8 °C/min with a non-optimized pin array in a vessel of 0.6L of Solar Salt. The current design of STEC could provide users with the expected 20,000 W/m^2 of flux a cooking temperature of 200 °C $\pm$ 20 °C for approximately 10 min. Typically, PCM's are of interest as a thermal solution due to their constant temperature during discharge. In the case of a relatively high heat flux

cooking device, the gradients significantly reduce usable temperature below the melting point of the PCM.

4.1.1 Recommendations

Exploring higher thermal conductivity phase change materials is key to reducing the thermal gradients in the phase change material. Quantifying the observed curvature in the solidification front of the FEM model with its impact on the heat extraction efficiency described in Equation (2.2) is an important as well. Optimization of the pin fin array could reduce the thermal gradients. Further developing an understanding of fundamental driving parameters with regards to arbitrarily defined temperature requirements, like those in Figure 1.1, would be valuable for the development of design metrics for rapid optimization of thermal energy storage systems including alternate configurations of STEC. Verification of the pin to salt interface resistance is also important as this interface may not be fully bonded during solidification. Also, the assumption that convection in negligible is inaccurate if the phase change material is in a large open cavity and begins solidification even slightly above the PCM's melting temperature. Convection in the liquid region may aid in flattening the phase change front since convection will pull heat from the bottom of the cavity to the heat spreader leading to re-melting of the more rapidly advancing solidification front.

Furthermore, the temperature and power requirements for cooking in a rural setting can vary widely depending on the food being cooked. For foods that are boiled, such as rice or curries, the temperature requirements are similar to the requirements of boiling water. Frying or grilling can require cooking surface temperatures in excess of 330 °C. STEC will

perform optimally at temperatures significantly below the melting temperature of the PCM in a high heat flux case. Thus, utilizing Solar Salt as the PCM yields a design for STEC that is ill suited for grilling or frying.

Exploring the impact of a variable thermal conductance element within STEC would also be valuable. Methods of controlling the thermal path from the phase change material with variable conductance components could not only allow for improved control of heat rate but also heat rate stability. Maintaining a more constant temperature and flux at discharge could be important for many applications. Exploring uses for low heat flux application for stored thermal energy beyond cooking could also be valuable. A proposal for further development of STEC is contained in the Phase II Bill & Melinda Gates foundation proposal contained in Appendix D.

References

[1] "India Cookstoves and Fuels Market Assessment." [Online]. Available: http://cleancookstoves.org/resources_files/india-cookstove-and-fuels-market-assessment.pdf. [Accessed: 19-Apr-2015].

[2] "WHO | Deaths and DALYs attributable to indoor air pollution (2002)."

[3] "The State of the Global Clean and Improved Cooking Sector." [Online]. Available: http://cleancookstoves.org/resources/380.html. [Accessed: 13-Jul-2015].

[4] N. V. Kkartchenko and V. M. Kkartchenko, "Thermal Energy Storage (TES) (Section 11.4)," in *Advanced Energy Systems, Second Edition*, CRC Press; 2 edition, 2013, pp. 421–427.

[5] T. Yan, R. Z. Wang, T. X. Li, L. W. Wang, and I. T. Fred, "A review of promising candidate reactions for chemical heat storage," *Renew. Sustain. Energy Rev.*, vol. 43, pp. 13–31, Mar. 2015.

[6] A. Sharma, V. V. Tyagi, C. R. Chen, and D. Buddhi, "Review on thermal energy storage with phase change materials and applications," *Renew. Sustain. Energy Rev.*, vol. 13, no. 2, pp. 318–345, Feb. 2009.

[7] K. Coscia, "Binary and Ternary Nitrate Solar Heat Transfer Fluids," *J. Sol. Energy Eng.*, vol. 135, no. 2, p. 021011, 2013.

[8] R. W. Bradshaw and N. P. Siegel, "Molten Nitrate Salt Development for Thermal Energy Storage in Parabolic Trough Solar Power Systems," in *ASME 2008 2nd International Conference on Energy Sustainability, Volume 2*, 2008, pp. 631–637.

[9] A. G. Fernández, M. Cortes, E. Fuentealba, and F. J. Pérez, "Corrosion properties of a ternary nitrate/nitrite molten salt in concentrated solar technology," *Renew. Energy*, vol. 80, pp. 177–183, Aug. 2015.

[10] C. W. Foong, O. J. Nydal, and J. Løvseth, "Investigation of a small scale double-reflector solar concentrating system with high temperature heat storage," *Appl. Therm. Eng.*, vol. 31, no. 10, pp. 1807–1815, 2011.

[11] G. J. Janz, B. Allen, Carolyn, N. P. Bansal, R. M. Murphy, and R. P. . Tomkins, "Physical Properties Data Compilations Relevant to Energy Storage. II. Molten Salts: Data on Single and Multi-Components Salt Systems," *National Bureau of Standards*. 1979.

[12] and R. P. T. T. G. J. Janz (Rensselaer Polytechnic Institute), H.F. Siegenthaler, “Molten Salts: Volume 3, Nitrates, Nitrites, and Mixtures.” National Istitute of Standards and Technology, Troy, N.Y. 12180, 1972.

[13] F. Roget, C. Favotto, and J. Rogez, “Study of the KNO3-LiNO3 and KNO3-NaNO3-LiNO3 eutectics as phase change materials for thermal storage in a low-temperature solar power plant,” *Sol. Energy*, vol. 95, pp. 155–169, 2013.

[14] L. . Chow, J. . Zhong, and J. . Beam, “Thermal conductivity enhancement for phase change storage media,” *Int. Commun. Heat Mass Transf.*, vol. 23, no. 1, pp. 91–100, Jan. 1996.

[15] D. Zhao and G. Tan, “Numerical analysis of a shell-and-tube latent heat storage unit with fins for air-conditioning application,” *Appl. Energy*, vol. 138, pp. 381–392, Jan. 2015.

[16] P. P. Levin, A. Shitzer, and G. Hetsroni, “Numerical optimization of a PCM-based heat sink with internal fins,” *Int. J. Heat Mass Transf.*, vol. 61, pp. 638–645, Jun. 2013.

[17] A. Sciacovelli, F. Gagliardi, and V. Verda, “Maximization of performance of a PCM latent heat storage system with innovative fins,” *Appl. Energy*, vol. 137, pp. 707–715, Jan. 2015.

[18] R. Baby and C. Balaji, “Thermal optimization of PCM based pin fin heat sinks: An experimental study,” *Appl. Therm. Eng.*, vol. 54, no. 1, pp. 65–77, May 2013.

[19] R. Akhilesh, A. Narasimhan, and C. Balaji, “Method to improve geometry for heat transfer enhancement in PCM composite heat sinks,” *Int. J. Heat Mass Transf.*, vol. 48, no. 13, pp. 2759–2770, Jun. 2005.

[20] N. H. S. Tay, F. Bruno, and M. Belusko, “Comparison of pinned and finned tubes in a phase change thermal energy storage system using CFD,” *Appl. Energy*, vol. 104, pp. 79–86, Apr. 2013.

[21] S. C. Fok, W. Shen, and F. L. Tan, “Cooling of portable hand-held electronic devices using phase change materials in finned heat sinks,” *Int. J. Therm. Sci.*, vol. 49, no. 1, pp. 109–117, Jan. 2010.

[22] W. Li, R. Zhang, N. Jiang, X. Tang, H. Shi, X. Zhang, Y. Zhang, L. Dong, and N. Zhang, “Composite macrocapsule of phase change materials/expanded graphite for thermal energy storage,” *Energy*, vol. 57, pp. 607–614, Aug. 2013.

[23] Y. J. Zhao, R. Z. Wang, L. W. Wang, and N. Yu, “Development of highly conductive KNO3/NaNO3 composite for TES (thermal energy storage),” *Energy*, vol. 70, pp. 272–277, Jun. 2014.

[24] H.-S. Kou, J.-J. Lee, and C.-Y. Lai, “Thermal Analysis and Optimum Fin Length of a Heat Sink,” *Heat Transf.*

Eng., vol. 24, no. 2, pp. 18–29, 2003.

[25] M. Bareiss and H. Beer, "Experimental investigation of melting heat transfer with regard to different geometric arrangements," *Int. Commun. Heat Mass Transf.*, vol. 11, no. 4, pp. 323–333, Jul. 1984.

[26] A. Gadgil and D. Gobin, "Analysis of Two-Dimensional Melting in Rectangular Enclosures in Presence of Convection," *J. Heat Transfer*, vol. 106, no. 1, p. 20, Feb. 1984.

[27] W. M. Deen, "Analysis of Transport Phenomena Ch 12: Transport in Bouyancy Driven Flow," 2nd ed., OUP USA, 1998, pp. pp. 464–476.

[28] A. Faghri and Y. Zhang, *Transport Phenomena in Multiphase Systems*. Burlington MA: Elsevier, 2006.

[29] A. Faghri and Y. Zhang, *Transport Phenomena in Multiphase Systems Ch 6: Melting and Solidification*. Elsevier, 2006.

[30] W. M. Deen, *Analysis of Transport Phenomena*, 2nd ed. OUP USA, 1998.

[31] A. Faghri and Y. Zhang, *Transport Phenomena in Multiphase Systems*. 2006.

[32] "LOW-TECH MAGAZINE: Well-Tended Fires Outperform Modern Cooking Stoves." [Online]. Available: http://www.lowtechmagazine.com/2014/06/thermal-efficiency-cooking-stoves.html. [Accessed: 23-Dec-2014].

[33] P. Arveson, "HotPot Solar Cooker," *Parveson (talk)*. [Online]. Available: https://en.wikipedia.org/wiki/File:HotPot_solar_cooker_with_panel_reflector_(5_liter_capacity,_front_view).png. [Accessed: 26-Jan-2016].

[34] D. R. Tobergte and S. Curtis, "HotPot Solar Cooker Reflector Optical Evaluation and Design Evolution," *J. Chem. Inf. Model.*, vol. 53, no. 9, pp. 1689–1699, 2013.

[35] N. H. Ravindranath and J. Ramakrishna, "Energy options for cooking in India," *Energy Policy*, vol. 25, no. 1, pp. 63–75, Jan. 1997.

[36] S. Foster, "Spherical Solar Stove: A Characterization Study MAE Project," pp. 1–24, 2015.

[37] M. J. Moran and H. N. Shapiro, "Properties Of Selected Solids and Liquids (Table A-19)," in *Fundamentals of Engineering Thermodynamics*, 5th ed., John Wiley & Sons, 2004.

[38] A. Faghri and Y. Zhang, "Transport Properties (Appendix B)," in *Transport Phenomena in Multiphase Systems*, Elsevier, 2006, pp. 954–1005.

Appendices

Appendix A: STEC Concept Drawings

Appendix B: Mathematica Code

Appendix C: Bill & Melinda Gates Foundation Phase I Grant Proposal and Phase I Scientific Report

Appendix D: Bill & Melinda Gates Foundation Phase II Proposal

Appendix E: ANSYS Model Example

Appendix A

Included in appendix A are conceptual drawings of a Stored Thermal Energy Cookstove that is designed to the specifications below. The drawings are conceptual and not intended to be used for manufacture.

STEC Drawings

Specifications for the 4th Generation Modular Design of STEC (2 discs + Vessel)

Specification	***Value***
Weight of Vessel and 2 Discs	12 lb (5.5 kg)
Nominal Cooking Surface Temperature	200 ºC (392 ºF)
Heating Rate	350 W
Cooking Surface Diameter	15.2 cm (6.00 in)
Boiling time for 1 liter of water	15 min
Simmering Time for 1 Liter of water (after bringing to a boil)	45 min
Recharge Time in collector @ 260C	2 hours
Daily Storage Time	10 hours

Appendix B

Included in Appendix B are links to the Mathematica notebooks utilized to develop the analytical relationships and generate the charts in the thesis.

Mathematica Initialization Parameters

Planar Solidification

Cylindrical Solidification

Compare Cylindrical and Planar Solidification

Temperature Dependent Enthalpy

Appendix C

Contained in Appendix C is the Phase I grant proposal to the Bill & Melinda Gates Foundation describing the initial concept and the Phase I Scientific Report which summarizes the key results of the two-year effort that started in October 2013.

Initial Phase I Proposal – Full text

Scientific and Financial Report – Full Text

Appendix D

Contained in Appendix D is the follow-up Phase II grant proposal submitted to the Bill & Melinda Gates Foundation on November 3rd 2015 which details a flexible pilot strategy proposed to continue development of STEC.

Bill and Melinda Gate Foundation Phase II Proposal – Full Text

Appendix E

Contained in Appendix E is a description of the mesh and model settings for the ANSYS FEM Transient Thermal model.

Product Version	15.0 Release
Save Project Before Solution	No
Save Project After Solution	No

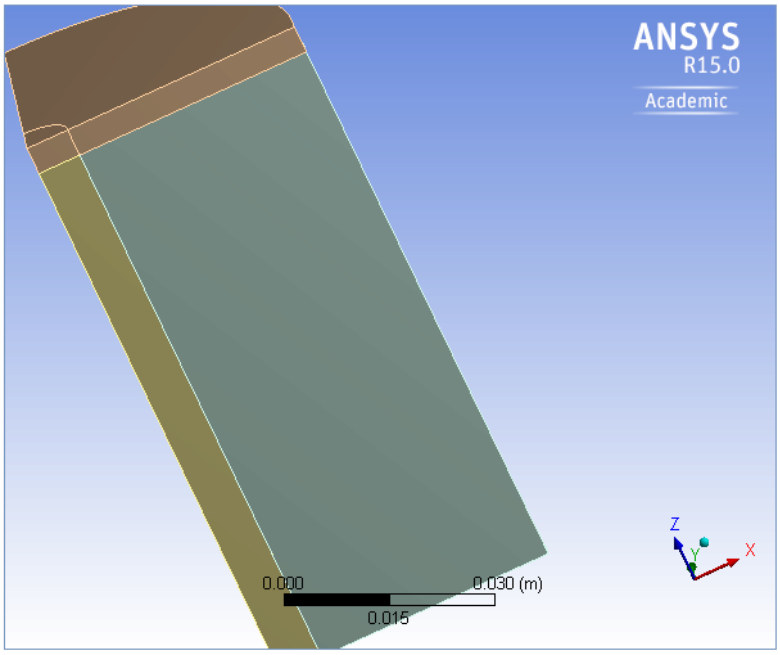

Geometry

Object Name	*Geometry*
State	Fully Defined
Definition	
Type	DesignModeler
Length Unit	Meters
Element Control	Program Controlled
Display Style	Body Color
Bounding Box	
Length X	4.18e-002 m
Length Y	4.18e-002 m
Length Z	8.778e-002 m
Properties	
Volume	1.2046e-004 m^3
Mass	0.22437 kg
Scale Factor Value	1.
Statistics	
Bodies	4
Active Bodies	4
Nodes	143556
Elements	32215
Mesh Metric	None
Basic Geometry Options	
Parameters	Yes
Parameter Key	DS
Attributes	No

Named Selections	No
Material Properties	No
Advanced Geometry Options	
Use Associativity	Yes
Coordinate Systems	No
Reader Mode Saves Updated File	No
Use Instances	Yes
Smart CAD Update	No
Compare Parts On Update	No
Attach File Via Temp File	Yes
Analysis Type	3-D
Decompose Disjoint Geometry	Yes
Enclosure and Symmetry Processing	Yes

TABLE 3
Model (C4) > Geometry > Parts

Object Name	*CookSurf*	*Salt*	*Pin*	*Pin*
State	Meshed			
Graphics Properties				
Visible	Yes			
Transparency	1			
Definition				
Suppressed	No			
Stiffness Behavior	Flexible			
Coordinate System	Default Coordinate System			
Reference Temperature	By Environment			

Material				
Assignment	Aluminum 6061	Sodium-Patassium Nitrate by Enthalpy	Aluminum 6061	
Nonlinear Effects	Yes			
Thermal Strain Effects	Yes			
Bounding Box				
Length X	4.18e-002 m		6.35e-003 m	
Length Y	4.18e-002 m		6.35e-003 m	
Length Z	4.18e-003 m	8.36e-002 m		4.18e-003 m
Properties				
Volume	5.6037e-006 m³	1.1207e-004 m³	2.6475e-006 m³	1.3238e-007 m³
Mass	1.513e-002 kg	0.20173 kg	7.1484e-003 kg	3.5742e-004 kg
Centroid X	-0.98192 m	-0.98194 m	-0.99731 m	
Centroid Y	1.0181 m		1.0027 m	
Centroid Z	2.09e-003 m	-4.18e-002 m		2.09e-003 m
Moment of Inertia Ip1	2.47e-006 kg·m²	1.4951e-004 kg·m²	4.1561e-006 kg·m²	1.2186e-009 kg·m²
Moment of Inertia Ip2	1.1752e-006 kg·m²	1.3231e-004 kg·m²	4.1681e-006 kg·m²	1.8191e-009 kg·m²
Moment of Inertia Ip3	3.6013e-006 kg·m²	4.7794e-005 kg·m²	3.9874e-008 kg·m²	2.0004e-009 kg·m²
Statistics				
Nodes	5885	132275	3808	1588
Elements	1200	30000	725	290
Mesh Metric	None			

Model (C4) > Construction Geometry

Object Name	*Construction Geometry*
State	Fully Defined
Display	
Show Mesh	No

Model (C4) > Construction Geometry > Paths

Object Name	*Salt Top*	*Pin Center*	*Salt Bottom*	*Salt Middle*	*Pin Center 2*	*CookSurface*
State	Fully Defined					
Definition						
Path Type	Edge	Two Points	Edge	Two Points	Edge	Two Points
Suppressed	No					
Path Coordinate System		Global Coordinate System		Global Coordinate System		Global Coordinate System
Number of Sampling Points		47.		47.		47.
Scope						
Geometry	1 Edge		1 Edge		1 Edge	
Start						
Coordinate System		Global Coordinate System		Global Coordinate System		Global Coordinate System
Start X Coordinate		-0.9975 m		-0.99365 m		-0.99365 m
Start Y Coordinate		1. m		1. m		1. m

Start Z Coordinate		0. m		-4.18e-002 m		5.e-003 m
Location		Defined		Defined		Defined
End						
Coordinate System		Global Coordinate System		Global Coordinate System		Global Coordinate System
End X Coordinate		-0.9975 m		-0.9582 m		-0.9582 m
End Y Coordinate		1. m		1. m		1. m
End Z Coordinate		-8.36e-002 m		-4.18e-002 m		5.e-003 m
Location		Defined		Defined		Defined

Model (C4) > Coordinate Systems > Coordinate System

Object Name	*Global Coordinate System*
State	Fully Defined
Definition	
Type	Cartesian
Coordinate System ID	0.
Origin	
Origin X	0. m
Origin Y	0. m
Origin Z	0. m
Directional Vectors	
X Axis Data	[1. 0. 0.]
Y Axis Data	[0. 1. 0.]
Z Axis Data	[0. 0. 1.]

Model (C4) > Mesh

Object Name	*Mesh*
State	Solved
Defaults	
Physics Preference	Mechanical
Relevance	0
Sizing	
Use Advanced Size Function	On: Curvature
Relevance Center	Fine
Initial Size Seed	Active Assembly
Smoothing	High
Transition	Fast
Span Angle Center	Fine
Curvature Normal Angle	Default (18.0 °)
Min Size	Default (1.545e-005 m)
Max Face Size	Default (1.545e-003 m)
Max Size	Default (3.0899e-003 m)
Growth Rate	Default (1.850)
Minimum Edge Length	4.18e-003 m
Inflation	
Use Automatic Inflation	None
Inflation Option	Smooth Transition
Transition Ratio	0.272
Maximum Layers	5
Growth Rate	1.2
Inflation Algorithm	Pre

View Advanced Options	No
Patch Conforming Options	
Triangle Surface Mesher	Program Controlled
Patch Independent Options	
Topology Checking	Yes
Advanced	
Number of CPUs for Parallel Part Meshing	Program Controlled
Shape Checking	Standard Mechanical
Element Midside Nodes	Program Controlled
Straight Sided Elements	No
Number of Retries	0
Extra Retries For Assembly	Yes
Rigid Body Behavior	Dimensionally Reduced
Mesh Morphing	Disabled
Defeaturing	
Pinch Tolerance	Default (1.3905e-005 m)
Generate Pinch on Refresh	No
Automatic Mesh Based Defeaturing	On
Defeaturing Tolerance	Default (7.7248e-006 m)
Statistics	
Nodes	143556
Elements	32215
Mesh Metric	None

Model (C4) > Mesh > Mesh Controls

Object Name	*X Sizing*	*Radial Sizing*	*Edge Sizing 3*	*Edge Sizing*	*Edge Sizing 4*	*X Sizing 2*
State	Fully Defined					
Scope						
Scoping Method	Geometry Selection					
Geometry	4 Edges	12 Edges	6 Edges	7 Edges	8 Edges	4 Edges
Definition						
Suppressed	No					
Type	Number of Divisions					
Number of Divisions	100	12	10	25	4	10
Behavior	Hard					
Bias Type	No Bias					

Model (C4) > Analysis

Object Name	*Transient Thermal (C5)*
State	Solved
Definition	
Physics Type	Thermal
Analysis Type	Transient
Solver Target	Mechanical APDL
Options	
Generate Input Only	No

Model (C4) > Transient Thermal (C5) > Initial Condition

Object Name	*Initial Temperature*
State	Fully Defined
Definition	

Initial Temperature	Uniform Temperature
Initial Temperature Value	222.5 °C

Model (C4) > Transient Thermal (C5) > Analysis Settings

Object Name	*Analysis Settings*
State	Fully Defined
Step Controls	
Number Of Steps	1.
Current Step Number	1.
Step End Time	3600. s
Auto Time Stepping	On
Define By	Time
Initial Time Step	3.6 s
Minimum Time Step	3.6 s
Maximum Time Step	360. s
Time Integration	On
Solver Controls	
Solver Type	Program Controlled
Radiosity Controls	
Radiosity Solver	Program Controlled
Flux Convergence	1.e-004
Maximum Iteration	1000.
Solver Tolerance	0.1 W/m²
Over Relaxation	0.1
Hemicube Resolution	10.
Nonlinear Controls	

Heat Convergence	Program Controlled
Temperature Convergence	Program Controlled
Line Search	On
Nonlinear Formulation	Full
Output Controls	
Calculate Thermal Flux	Yes
General Miscellaneous	No
Store Results At	All Time Points
Analysis Data Management	
Future Analysis	None
Scratch Solver Files Directory	
Save MAPDL db	No
Delete Unneeded Files	Yes
Nonlinear Solution	Yes
Solver Units	Active System
Solver Unit System	mks

Model (C4) > Transient Thermal (C5) > Loads

Object Name	*Convection*
State	Fully Defined
Definition	
Type	Convection
Film Coefficient	100. W/m²·°C (step applied)
Ambient Temperature	20. °C (step applied)